Please cite this article in press as: Kaneko et al., Interactions between JARID2 and Noncoding RNAs Regulate PRC2 Recruitment to Chromatin, Molecular Cell (2014), http://dx.doi.org/10.1016/j.molcel.2013.11.012

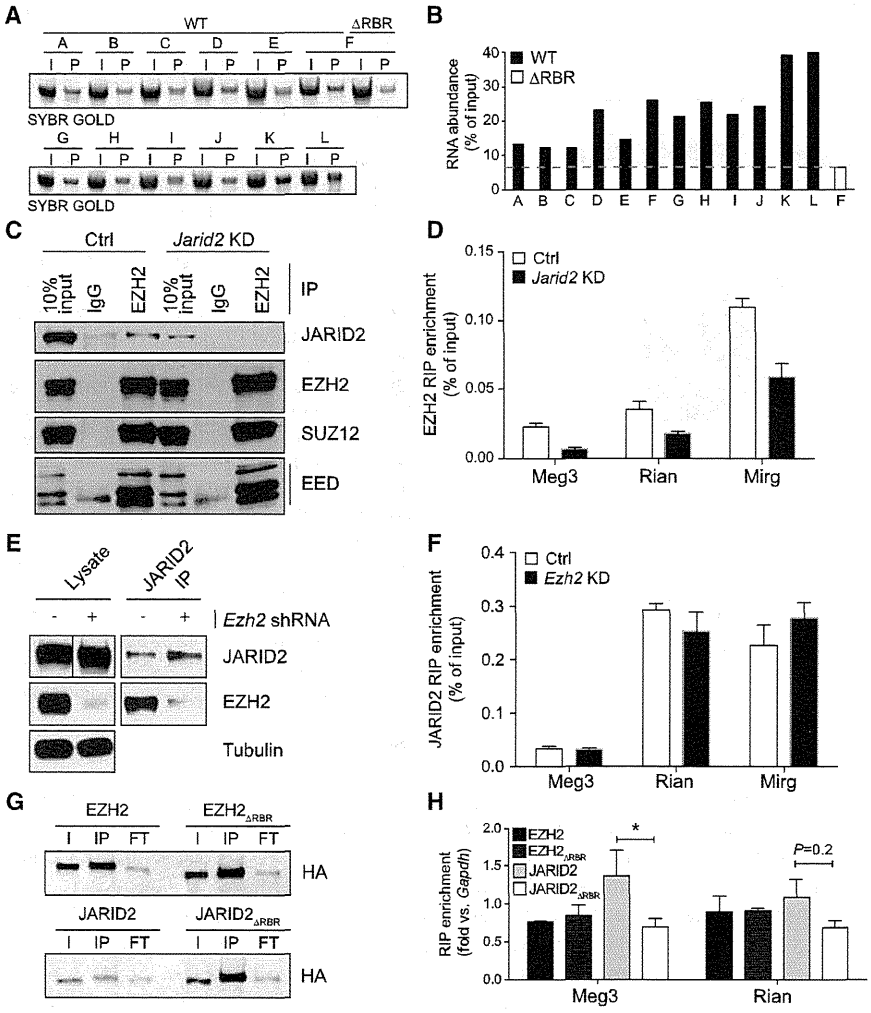

Figure 3. The JARID2 RBR Mediates Interactions of Meg3 with PRC2

(A) In vitro pull-down assay with different fragments of Meg3 using 4 μg of GST-JARID2 119–450 WT or ΔRBR.

(B) Quantification of bands shown in (A).

(C) RIPs for EZH2 were performed in E14 ESCs stably transfected with an shRNA against *Jarid2* (KD) or empty vector (ctrl). Coprecipitated proteins were revealed by western blot. The 10% input and IgG lanes are shown as controls.

(D) qRT-PCR on EZH2 RIPs from control E14 ESCs (white bars) or *Jarid2* knockdown E14 ESCs (black bars). Data are shown as percentage of RIP input. Bars represent the mean of four replicates + SD.

(E and F) As in (C) and (D) but *Ezh2* was knocked down and the RIP were performed with JARID2 antibodies.

(G) Western blots for HA RIPs from nuclear extracts of KH2 transiently transfected with N3-tagged EZH2, $EZH2_{\Delta RBR}$ (top), JARID2, and $JARID2_{\Delta RBR}$ (bottom). I, input; IP, HA immunoprecipitation; FT, flow-through.

(H) qRT-PCR normalized to *Gapdh* levels on HA RIPs described in (E). Bars indicate the mean of three biological replicates + SEM. *p < 0.05 by Mann-Whitney *U* test.

See also Figures S3 and S4.

The RBR of JARID2 Contributes to Meg3 Binding In Vitro and In Vivo

Having identified Meg3 as a JARID2-interacting lncRNA by CLIP, we next tested this interaction in vitro. We performed pull-down assays with in vitro-transcribed fragments of Meg3 (Figure 2G, bottom) obtained from a previously generated clone (Zhao et al., 2010). Although all tested fragments bound to a recombinant JARID2 fragment spanning the RBR (Figure 3A), the interaction was stronger for fragments originating from the 3′ end of the clone (Figure 3B), including one (fragment "K") that spanned the only RCS identified in this region (Figure 2G). We analyzed structural predictions for these fragments but found no obvious similarities among those that bound with higher affinity, except a trend for less stable structures (Figure S3). Importantly, a JARID2 fragment lacking the RBR displayed a pronounced reduction in binding affinity, at least toward the Meg3 fragment tested (fragment "F"; Figures 3A and 3B).

To validate these JARID2-RNA interactions with a technique more quantitative than PAR-CLIP, we resorted to native RNA immunoprecipitations (RIPs) followed by quantitative PCR (qPCR). Consistent with our PAR-CLIP results and previous reports (Zhao et al., 2010), Meg3 was enriched in PRC2 RIPs performed with EZH2 antibodies, and so were two other lncRNAs encoded within the same imprinted locus, Rian and Mirg (Figures 3C and 3D). However, when we depleted JARID2 by small hairpin RNA (shRNA)-mediated knockdown, we observed a considerable decrease in the amounts of these lncRNAs coprecipitating with PRC2 (Figures 3C and 3D), and similar results were obtained with SUZ12 antibodies (Figures S4A and S4B). Importantly, knockdown of *Ezh2* did not affect the ability of JARID2 to bind to Meg3, Rian, or Mirg (Figures 3E and 3F), suggesting that the JARID2-Meg3 interaction makes the largest contribution to the affinity of Meg3 for PRC2.

We then asked whether Meg3 bound to JARID2 via the RBR. To this end, we transiently expressed in mouse ESCs hemagglutinin (HA)-tagged EZH2, EZH2 lacking the previously identified RBR ($EZH2_{\Delta RBR}$) (Kaneko et al., 2010), JARID2, and $JARID2_{\Delta RBR}$ and performed HA RIPs followed by quantitative RT-PCRs (qRT-PCRs). Consistent with the results presented above, the interaction of Meg3 with JARID2 was significantly decreased when its RBR was removed, whereas EZH2 and $EZH2_{\Delta RBR}$ coprecipitated Meg3 with equal efficiencies (Figures 3G and 3H). We detected a similar trend for Rian, although in that case the difference did not reach statistical significance (Figure 3H). Similarly, human JARID2, but not human $JARID2_{\Delta RBR}$, bound to Meg3 in mouse ESCs (Figures S4C and S4D).

These data supported the conclusion that Meg3 interacts with PRC2 mainly through the RBR of JARID2, which led us to speculate that this lncRNA may participate in the function of JARID2 on chromatin.

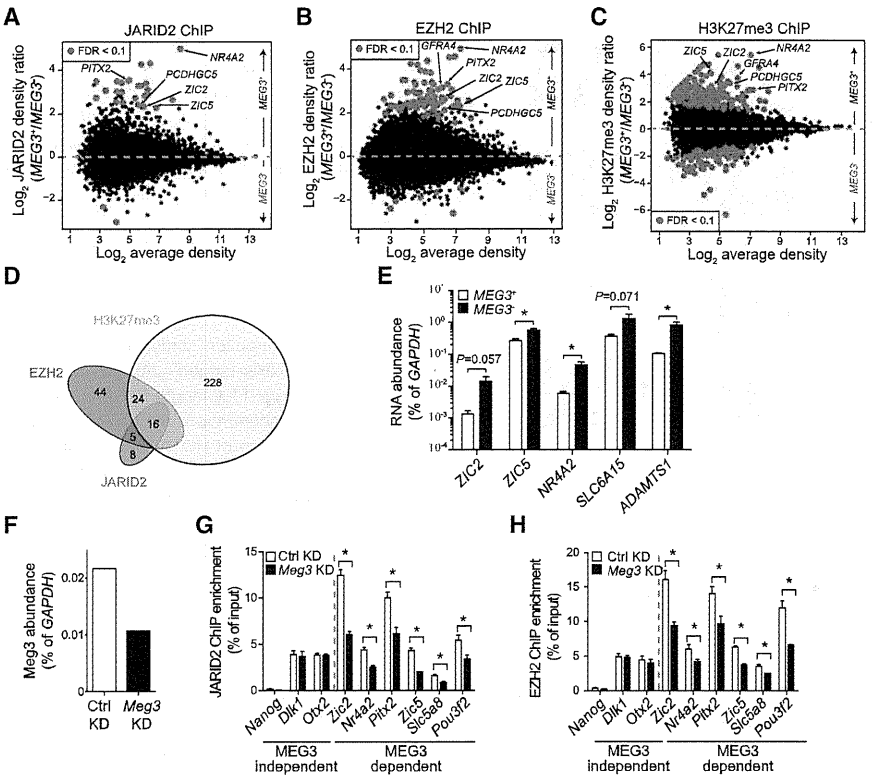

Figure 4. Decreased Occupancy of PRC2 at Some Chromatin Targets in *MEG3*$^-$ Cells

(A–C) MA plots for JARID2 (A), EZH2 (B), and H3K27me3 (C) occupancy, as determined by the normalized and input-corrected read densities in *MEG3*$^+$ (above dotted line) versus *MEG3*$^-$ (below dotted line) hiPSC lines. Each dot represents an ER in common between at least two hiPSC lines. DBRs with an FDR < 0.1 are displayed in red.

(D) Venn diagram for DBRs with FDR < 0.1.

(E) qRT-PCR analysis of PRC2 targets in *MEG3*$^+$ and *MEG3*$^-$ hiPSCs. Bars represent the mean RNA abundance (as percentage of *GAPDH*) in the five *MEG3*$^+$ and three *MEG3*$^-$ lines tested. *p < 0.05, as calculated by Mann-Whitney *U* test.

(F) qRT-PCR for *Meg3* 24 hr after transfection of KH2 ESCs with control (white bar) or *Meg3* siRNAs.

(G and H) ChIP-qPCR for JARID2 (G) or EZH2 (H) with primers mapping to PRC2 peaks near the indicated genes in KH2 ESCs treated with control (white bars) or *Meg3* (black bars) siRNAs. Bars represent the mean of three replicates + SEM. *p < 0.05 by Mann-Whitney *U* test.

See also Figures S5–S7 and Tables S2 and S3.

MEG3 Regulates PRC2 Occupancy In *Trans*

In light of the connection between MEG3 and pluripotency (Stadtfeld et al., 2010), we turned our attention to a set of eight human induced pluripotent stem cell (hiPSC) lines that differ greatly in their levels of *MEG3* expression (Nishino et al., 2011), thus offering a natural experimental system in which to study the effects of MEG3 on PRC2 function. We classified these lines into 5 *MEG3*$^+$ and 3 *MEG3*$^-$ (Figures S5A and S5B) and confirmed that *EZH2*, *SUZ12*, and *JARID2* were expressed at similar levels in *MEG3*$^+$ and *MEG3*$^-$ lines (Figures S5C–S5E). Importantly, pluripotent markers *OCT3/4* and *NANOG* were also expressed at comparable levels in all lines and at much higher levels than in differentiated cells, such as foreskin fibroblasts (Figures S5F and S5G).

Next, we performed chromatin immunoprecipitation (ChIP) followed by deep sequencing (ChIP-seq) for JARID2, EZH2, and H3K27me3, the product of PRC2 catalysis. We identified enriched regions (ERs) for all three features and compared normalized read densities in *MEG3*$^+$ versus *MEG3*$^-$ cells. The genome-wide analysis revealed 29, 89, and 268 differentially bound regions (DBRs) with a false discovery rate (FDR) < 0.1 in *MEG3*$^+$ versus *MEG3*$^-$ cells for JARID2, EZH2, and H3K27me3, respectively (Figures 4A–4C). At most of these *MEG3*-dependent DBRs, PRC2 exhibited stronger binding in the hiPSC lines that expressed *MEG3*, suggesting that the lncRNA had a stimulatory function (Figures 4A–4C; Figures S6A–S6C). Genes near the *MEG3*-dependent DBRs were enriched for functional terms related to the regulation of transcription during embryonic development and differentiation (Table S2), even taking into account the enrichment of developmental and transcription-related terms in the background population comprising all JARID2, EZH2, and H3K27me3 ERs (Table S3).

Of the 29 *MEG3*-dependent DBRs for JARID2, 21 overlapped with EZH2 DBRs (Figure 4D), and of these 16 also overlapped with H3K27me3 DBRs, a fraction much larger than expected by chance alone (p value < 10^{-20}, hypergeometric distribution). Among the regions with lower JARID2 occupancy in the absence of *MEG3* were the loci encoding the transcription factors *ZIC5*, *NR4A2*, *ZIC2*, and *PITX*, as well as the neuronal gene *PCDHGC5* (Figure S6D and data not shown), all of which function in differentiating or differentiated cells and must therefore be silenced in pluripotent stem cells. In all loci tested, the *MEG3*-dependent loss of PRC2 targeting resulted in transcriptional derepression (Figure 4E).

It has been suggested that, in mouse ESCs, Meg3 exerts a *cis*-repressive effect on the adjacent *Dlk1* gene by recruiting PRC2 (Zhao et al., 2010). To determine whether a similar mechanism was conserved in hiPSCs, we analyzed the *DLK1* promoter in *MEG3*$^+$ versus *MEG3*$^-$ hiPSCs. Unexpectedly, we observed no differences in JARID2 or PRC2 occupancy (data not shown) and no evidence of a reciprocal correlation in the levels of *MEG3* and *DLK1* RNA in these cells (Figure S5H) or with the protein-coding RNA at the other extremity of the imprinted locus, *DIO3* (Figure S5J).

Because the *DLK1-DIO3* locus encodes multiple ncRNAs (*MEG3*, *RIAN*, and *MIRG*), all repressed in *MEG3*$^-$ hiPSCs, we examined the effect of altering *MEG3* levels alone on PRC2 localization. We overexpressed *MEG3* (or GFP RNA as a control) in *MEG3*$^-$ hiPSCs and analyzed the distribution of JARID2 and EZH2 by ChIP-seq. A caveat of this experiment is that *MEG3* was expressed at levels ~10 times higher than in the average *MEG3*$^+$ line (Figure S7A); nonetheless, we observed increased

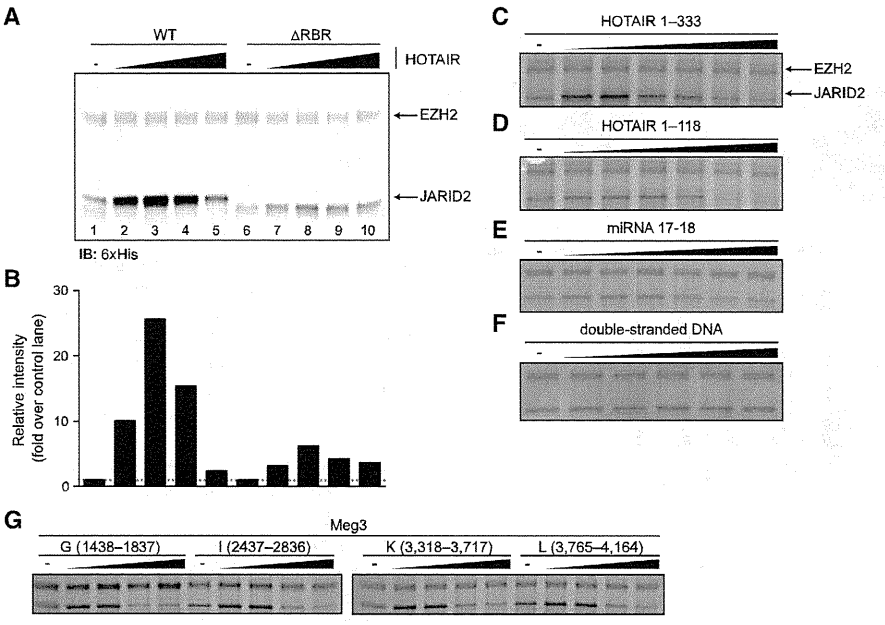

Figure 5. HOTAIR Stimulates EZH2–JARID2 Interactions via the JARID2 RBR

(A) FLAG-6xHis-tagged recombinant EZH2 (20 pmol) was incubated with 6xHis-tagged $JARID2_{119–450}$ WT or ΔRBR (40 pmol) in presence of increasing amounts of $HOTAIR_{1–333}$ (0–12 pmol). Pull-down was performed with anti-FLAG beads and proteins revealed by 6xHis immunoblot.

(B) Densitometric quantification of the signal for JARID2 shown in (A). WT and ΔRBR lanes were normalized each to lane 1 and lane 6 (no HOTAIR control), respectively.

(C–F) In vitro interaction stimulation assays with recombinant 6xHis-tagged $JARID2_{119–574}$ and FLAG-6xHis-tagged full-length EZH2 in presence of increasing concentrations of $HOTAIR_{1–333}$ (C), a smaller 5′ truncation of HOTAIR (D), a microRNA (E), or double-stranded DNA (F). Pull down was performed with anti-FLAG beads and proteins stained with Coomassie blue.

(G) Same as (C)–(F) using Meg3 fragments.

densities of JARID2 at some *MEG3*-dependent DBRs, but not at control targets (Figure S7B). However, we did not detect recovery of JARID2 occupancy at all JARID2 DBRs (Figure S7C), suggesting that the regulation afforded by endogenous MEG3 could not be fully recapitulated by providing large amounts of the lncRNA in *trans*. Interestingly, PRC2 was preferentially depleted from the EZH2 DBRs upon overexpression of *MEG3* (Figure S7D). Although this depletion of EZH2 was unexpected, the fact that the EZH2 DBRs were preferentially depleted by the manipulation of MEG3 levels is consistent with the idea that occupancy at these sites is selectively regulated by this lncRNA.

To further verify that the observed changes in PRC2 occupancy were directly related to the changes in MEG3 levels, we performed transient knockdown of the orthologous lncRNA in mouse ESCs. Despite only partial knockdown efficiency (~50%; Figure 4F), six out of nine DBRs tested lost JARID2 and EZH2 after Meg3 depletion (Figures 4G and 4H), suggesting that the regulation of PRC2 by Meg3 is conserved between human and mouse. PRC2 occupancy at *Plek2*, *Mbnl3*, and *Cdx4* was not affected by *Meg3* knockdown (data not shown), despite the fact that orthologous loci were among the MEG3-dependent DBRs in hiPSCs. However, it is not surprising that subtle differences in gene regulation would exist across this species barrier, especially given that mouse and human stem cells are not equivalent (Ginis et al., 2004).

Together, our ChIP experiments in hiPSCs and mouse ESCs support the conclusion that MEG3 acts in *trans* on PRC2 and JARID2 by facilitating their recruitment to a subset of target genes.

RNA Facilitates JARID2-PRC2 Interactions

Given that loss of MEG3 caused defects in PRC2 recruitment and that several lncRNAs crosslinked to both JARID2 and EZH2 in vivo, we hypothesized that RNA-mediated scaffolding could stabilize JARID2-PRC2 interactions. To test this hypothesis in vitro, we first examined the lncRNA HOTAIR, which functions as a scaffold between the LSD1/CoREST/REST complex and PRC2 (Tsai et al., 2010). Low amounts of HOTAIR stimulated the interaction between recombinant EZH2 and JARID2 fragments in vitro (Figures 5A and 5B, compare lanes 1–3), whereas higher concentrations of the RNA resulted in a return to baseline interaction levels, suggesting the possibility of squelching (Figures 5A and 5B, compare lanes 3–5). This stimulation was considerably reduced for JARID2 fragments that lacked the RBR (Figures 5A and 5B, lanes 6–10) but retained the ability to interact with EZH2 (Figure 5A, compare lanes 1 and 6) or when we replaced the HOTAIR lncRNA fragment with a shorter version, a control pre-microRNA that forms two stem-loops, or double-stranded DNA containing the HOTAIR lncRNA sequence (Figures 5C–5F). Stimulation of binding was also observed when we incubated recombinant EZH2 and JARID2 with those Meg3 fragments that displayed maximum affinity in the in vitro pull-down assay (Figure 5G). Therefore, stimulation of JARID2-EZH2 interactions may be a general mechanism of action for lncRNAs that bind to these proteins.

The JARID2 RBR Stimulates PRC2 Assembly on Chromatin

Having discovered that lncRNAs stimulate JARID2-PRC2 interactions in vivo (Figure 4) and in vitro (Figure 5) and knowing that the RBR was required for the latter (Figures 5A and 5B), we asked whether it was also required for the former. To this end, we overexpressed JARID2 or $JARID2_{\Delta RBR}$ in human foreskin fibroblasts, which express high levels of *HOTAIR* (Rinn et al., 2007), and measured its accumulation at known genomic targets by ChIP-qPCR. Wild-type (WT) and mutant JARID2 were expressed at comparable levels in lentivirally transduced fibroblasts (Figure 6A, top) and did not affect EZH2 levels (Figure 6A, middle). Upon JARID2 overexpression, we observed increased accumulation

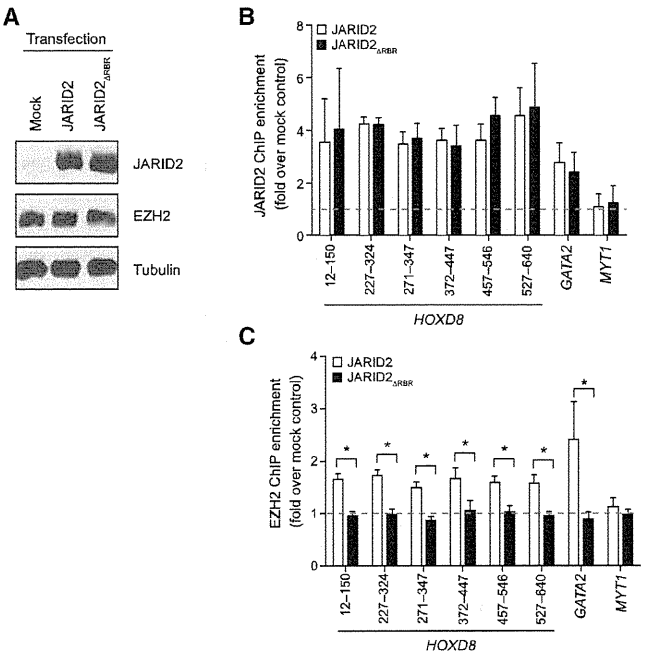

Figure 6. JARID2 Recruits EZH2 to Chromatin in an RBR-Dependent Manner

(A) Western blots for foreskin fibroblasts transduced with lentiviruses expressing JARID2, JARID2$_{\Delta RBR}$, or mock transduced.

(B and C) ChIP-qPCR with antibodies against JARID2 (B) or EZH2 (C) at known PRC2 chromatin targets in foreskin fibroblasts transduced as in (A). Several primer sets are shown for *HOXD8*. The primers for *MYT1* were designed at a distal location, devoid of PRC2, and serve as a negative control. The ChIP enrichment is normalized against that obtained with the same antibodies in mock-transfected control cells (dotted line). Bars represent mean of four technical replicates + SD (B) or three biological replicates + SEM (C). *$p < 0.05$ by Mann-Whitney *U* test.

of the protein at known chromatin targets, such as *HOXD8* and *GATA2*, compared with controls (Figure 6B). JARID2$_{\Delta RBR}$ accumulated at these targets with the same efficiency as the WT protein but, unlike the WT, it was incapable to recruit additional EZH2, which remained at the same levels as observed in the mock-transfected cells (Figure 6C). Given that these targets were already silent in the mock-transfected controls, we did not attempt to detect further repression at the transcriptional level.

These results suggest that RNA-protein interactions via the JARID2 RBR contribute to the recruitment and assembly of PRC2 on chromatin. Interestingly, depletion of HOTAIR in foreskin fibroblasts also impairs PRC2 recruitment at these loci (Rinn et al., 2007; Tsai et al., 2010), suggesting that it may act through interactions with the JARID2 RBR.

The fact that JARID2$_{\Delta RBR}$ is incapable of recruiting EZH2 to target sites is compatible with a model by which lncRNAs modulate JARID2-PRC2 interactions and orchestrate the distribution and activity of PRC2 on chromatin.

DISCUSSION

The results presented above allow us to add JARID2 to the growing list of chromatin-associated proteins that interact with lncRNAs and offer further support to the hypothesis that lncRNAs are a component of the *Polycomb* axis in mammals.

We mapped the JARID2 RBR to an N-terminal fragment that contains no annotated features or domains, despite the fact that, in addition to RNA binding, it is also responsible for interactions with SUZ12, EZH2, nucleosomes, and PRC2 stimulation (Kim et al., 2003; Li et al., 2010; Pasini et al., 2010; Son et al., 2013). Although we assigned these biochemical activities to distinct protein fragments (Figure S1), they do map to adjacent regions, and it is tempting to speculate that this vicinity might reflect a functional crosstalk, by which, for example, RNA binding could stimulate nucleosomal binding and contribute to PRC2 regulation.

Among the lncRNAs identified by PAR-CLIP, we focused our functional analysis on Meg3 because of its connections with ESC pluripotency, imprinting, and PRC2 function (da Rocha et al., 2008; Stadtfeld et al., 2010; Zhao et al., 2010). We demonstrated JARID2-Meg3 interactions using RIP-qPCR, PAR-CLIP, and in vitro pull-down assays. Importantly, we also found RCSs for EZH2 within *Meg3* in our previously published EZH2 PAR-CLIP data set (Kaneko et al., 2013) (Figures 2F and 2G). This is consistent with earlier results obtained by native and UV-cross-linked RIP (Zhao et al., 2010) and supports a model by which Meg3 contacts both JARID2 and EZH2 and stimulates their interaction. Without JARID2 the interaction between Meg3 and PRC2 is much weaker (Figure 3D), suggesting that of the two contact points, the one on JARID2 makes the larger contribution to the affinity for Meg3. We note that by using *Ezh2*$^{-/-}$ cells as a control, Zhao et al. could not have detected this requirement for JARID2, because in absence of EZH2 the IP performed with an anti-EZH2 antibody would not have recovered JARID2.

We envision a model in which some lncRNAs function as scaffold to stimulate assembly of PRC2 at JARID2 target sites (Figure 7A). In addition, the existence of DBRs that lose JARID2 occupancy in absence of MEG3 (Figure 4A) suggests that, at certain sites, lncRNAs might also be required for the initial recruitment of JARID2 (Figure 7B). In both scenarios, the net result of lncRNA action is to increase PRC2 occupancy and H3K27me3 deposition (Figures 7A and 7B). We have demonstrated this model using MEG3 and genomic targets in hiPSCs and mouse ESCs (Figure 4); however, the recovery of other lncRNAs cross-linked to both JARID2 and EZH2 by PAR-CLIP-seq (Figure 2F; Table S1) allows us to speculate that this mode of action might not be limited to MEG3. In fact, the JARID2$_{\Delta RBR}$ mutant does not recruit PRC2 to the *HOX* locus in foreskin fibroblasts, despite the fact that this locus is not MEG3 dependent. We propose that other lncRNAs function as scaffold for JARID2-PRC2 interactions in this setting and we note that foreskin fibroblasts express high levels of *HOTAIR* (Rinn et al., 2007), which is also able to stimulate JARID2-EZH2 interactions in vitro (Figure 5).

Not all lncRNAs bind equally to JARID2 and EZH2. Our reanalysis of EZH2 PAR-CLIP tags (Kaneko et al., 2013) identified a number of lncRNAs not shared with JARID2 (Figure 2F; Table S1) that, likely, regulate PRC2 function in JARID2-independent ways. In addition to lncRNAs, EZH2 binds to a variety of coding transcripts in vivo and in vitro with high affinity but seemingly low specificity (Davidovich et al., 2013; Kaneko et al., 2013). Those interactions appear to constitute a distinct regulatory

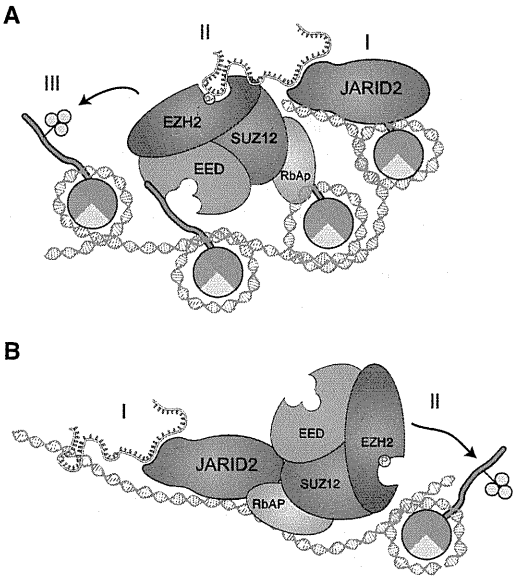

Figure 7. Proposed Model for the Interplay of lncRNAs, JARID2, and PRC2

(A) At some target genes, the presence of JARID2 by itself (I) is not sufficient for maximum PRC2 recruitment, which requires scaffolding by lncRNAs (II). The presence of both JARID2 and lncRNAs stimulates further recruitment and assembly of PRC2 on chromatin, resulting in increased H3K27me3 (III). The structure of lncRNAs bound to JARID2 (and PRC2) remains to be elucidated, and the one shown here is only for the purpose of illustration.

(B) In some cases, lncRNAs might contribute to the initial recruitment of JARID2 to chromatin (I). Because JARID2 also binds PRC2 via protein-protein interactions, this results in increased PRC2 recruitment and H3K27 methylation (II).

mechanism from the one described here, as they occur mostly at promoters of transcribed genes, which have low PRC2 occupancy (Davidovich et al., 2013; Kaneko et al., 2013) and are largely devoid of JARID2 (data not shown). However, we cannot exclude that nascent RNAs could compete with lncRNAs for binding to EZH2, which might help explain their apparent inhibitory function.

Our gain-of-function experiments in hiPSCs confirmed that at least some JARID2 DBRs identified in *MEG3*$^+$ versus *MEG3*$^-$ hiPSCs can be rescued by supplying MEG3 lncRNA in *trans* to otherwise *MEG3*-negative hiPSCs (Figure S7B). The ectopic expression of MEG3 lncRNAs caused EZH2 depletion rather than increased occupancy at the previously identified MEG3-dependent DBRs (Figure S7D), which was in contrast to our expectations. However, considering that lentiviral transduction resulted in 10-fold higher *MEG3* levels compared to endogenous *MEG3* (Figure S7A), we speculate that such an excess of RNA molecules acted in a dominant negative fashion through squelching, as seen in vitro (Figure 5). It is also possible that the random integration of the lentivirally encoded *MEG3* at ectopical sites within the genome may explain its unphysiological behavior in these experiments, given that the genomic location of lncRNA genes appears to play a pivotal role in their function (Ulitsky et al., 2011). Nonetheless, the fact that MEG3-dependent DBRs were selectively affected confirmed that occupancy at these targets is indeed regulated by MEG3, which was further supported by the results of transient *Meg3* knockdown in mouse ESCs (Figures 4G and 4H).

Genomic imprinting of *MEG3* is unstable in human ESCs, and several hiPSC lines, regardless of their parental cell type, maintain repression at this locus even after continuous passaging (Nishino et al., 2011). This is likely mediated by aberrant DNA hypermethylation (Nishino et al., 2011) (data not shown). Therefore, it is possible that current reprogramming protocols fail to set the appropriate epigenetic state at the *DLK1-DIO3* locus, which is an important consideration given that improper regulation of this imprinted regions leads to developmental abnormalities in mice (Stadtfeld et al., 2010; Takahashi et al., 2009) and humans (Kagami et al., 2008). The mechanistic details of the epigenetic alteration at this imprinted locus during reprogramming remains elusive, but our data suggest that MEG3 interactions with PRC2 might play an important role.

Although our findings suggest a molecular mechanism by which MEG3 contributes to JARID2 and PRC2 function, further investigations are required to address (1) whether and how this mechanism extends to the other lncRNAs identified by PAR-CLIP, and (2) whether and how lncRNAs regulate de novo recruitment of their interacting proteins to distant loci. Our in vitro binding analyses of Meg3 lncRNA suggest that JARID2 does not bind to RNA in a sequence-specific manner, consistent with the fact that the primary sequence of lncRNAs is not well conserved (Ulitsky et al., 2011).

In conclusion, we have demonstrated that JARID2, an essential regulatory component of PRC2 in pluripotent stem cells, contains an RNA-binding region that mediates, at least in part, its interaction with the imprinted lncRNA MEG3. This—and possibly other—RNA interaction contributes to proper recruitment and assembly of PRC2 on target genes and likely plays an important role in orchestrating the epigenetic regulation of gene expression that accompanies the transition from stem cell pluripotency to differentiation.

EXPERIMENTAL PROCEDURES

For information about antibodies, oligonucleotides, and plasmids see Tables S4–S6 and the Supplemental Experimental Procedures.

Cells

HiPSCs were cultured as described previously (Nishino et al., 2011). Cells were harvested at passage 34 (UtE-iPS-4), 41 (UtE-iPS-11), 45 (UtE-iPS-7), 41 (AM-iPS-6), 50 (AM-iPS-8), 39 (UtE-iPS-6), 41 (MRC5-iPS-25), and 90 (Edom-iPS-2). Human foreskin fibroblasts (#PCS-201-010, lot# 58490326; ATCC) were cultured in fibroblast basal medium (ATCC) plus fibroblast growth kit-low serum (ATCC). KH2 ESCs expressing the reverse tetracycline-controlled transactivator (rtTA) (Hochedlinger et al., 2005) were maintained in standard mouse ESC (mESC) culture conditions. KH2 lines expressing *Jarid2* and *Jarid2*$_{\Delta RBR}$ were generated by transfection of the relevant pINTA-N3 construct and selecting with 50 μg/ml Zeocin (Invitrogen). Transgene expression was induced with doxycycline for 24 hr. E14Tg2A.4 mESC lines (E14 mESC) and HEK293 and HEK293T cells were cultured as described previously (Kaneko et al., 2010). *Jarid2* knockdown mESCs were described previously (Li et al., 2010).

In Vitro Binding Assays

Protein purification, synthesis of HOTAIR lncRNA (1–333), and biotinylated RNA pull-down assays were described previously (Kaneko et al., 2010). All

RNA fragments were generated by in vitro transcription; see the Supplemental Information for details.

LncRNA-mediated stimulation of EZH2–JARID2 interactions was assayed by incubating FLAG- and 6xHis-tagged EZH2 (20 pmol) with increasing amounts (0–12 pmol) of lncRNAs in 100 µl of binding buffer (50 mM Tris-HCl, pH 7.9; 100 mM KCl; 0.1% NP-40) for 30 min at 25°C. 6xHis-tagged truncated JARID2 (40 pmol) was added to the reaction and incubated for 30 min at 25°C. Complexes were purified using FLAG-M2 affinity gel (Sigma), after washing with binding buffer.

For JARID2–Meg3 in vitro binding assays, 4 µg of GST-JARID2$_{119–450}$ were incubated with a series of Meg3 fragments (1 µg, 400 nt each; see Table S7). Bound RNAs were purified with glutathione beads, resolved with 7M urea gels, stained with SYBR-gold (Invitrogen), and quantified with an ImageQuant LAS4000 (GE Healthcare Life Sciences).

Knockdowns

For conditional knockdown of *Ezh2* in E14 mESCs, we generated stable clones with an integration of pTRIPZ lentiviral inducible shRNAmir targeting human and mouse *Ezh2* (#RHS4696-99635303; Open Biosystems). Selection was done by puromycin (1 µg/ml) and clones were screened by red fluorescent protein (RFP) expression after 3–4 days of doxycycline (1 µg/ml) induction.

For transient knockdown of *Meg3*, we tested four siRNAs from QIAGEN (SI05169486, SI05169710, SI01060129, and SI01060136) and used the siRNA resulting in the most efficient knockdown (SI05169486) (see Supplemental Information).

ChIP

ChIP from hiPSCs, foreskin fibroblast, and mESCs was performed as described (Kaneko et al., 2007), with minor modification, and libraries were constructed as described (Gao et al., 2012). Briefly, cells were crosslinked with 1% formaldehyde for 10 min and sonicated in ChIP buffer (50 mM Tris-HCl [pH 7.9], 150 mM NaCl, 1% Triton X-100, 0.5% NP-40, 5 mM EDTA [pH 8.0], 1 mM phenylmethanesulfonylfluoride, and protease inhibitors) with a Diagenode Bioruptor. Incubations with antibodies were carried out in an ultrasonic water bath for 30 min at 4°C. Samples were decrosslinked at 65°C for ~16 hr for library construction or 95°C 10 min for ChIP-qPCR. See the Supplemental Information for more details.

RNA Immunoprecipitation

For Figures 3G and 3H, nuclear extracts were obtained using an established protocol (Dignam et al., 1983) with minor modifications to minimize RNase activity, lysates were diluted in RIP buffer (20 mM Tris [pH 7.9]$_{4°C}$, 200 mM KCl, 0.05% IGEPAL CA-630, 10 mM EDTA), cleared by centrifugation at 20,000 × *g* for 10 min, and incubated with depleting amounts of antibody for 3 hr at 4°C. Immunocomplexes were recovered with protein G-coupled dynabeads (Invitrogen) for 1 hr at 4°C. Beads were washed in RIP-W buffer (20 mM Tris [pH 7.9]$_{4°C}$, 200 mM KCl, 0.05% IGEPAL CA-630, 1 mM $MgCl_2$) twice and incubated with 2 U TURBO DNase (Ambion) in 20 µl RIP-W buffer for 10 min at room temperature to avoid DNA bridging artifacts. After two additional washes, RNA was eluted and purified with TRIzol (Invitrogen).

For Figures 2C–2F, RIPs were performed on whole-cell lysates, as described before (Kaneko et al., 2010) (see also Supplemental Information).

ChIP-Seq Analysis

Sequenced reads from ChIP-seq experiments were mapped with BOWTIE using parameters -v2 -m4–best (Langmead et al., 2009). Normalized genome-wide read densities were computed and visualized on the UCSC genome browser. Bound regions (ERs) were identified using MACS 2.09 (Zhang et al., 2008) and default parameters. ERs were associated to gene targets using ChIPpeakAnno and ENSEMBL annotation 67.

PAR-CLIP

ESCs were pulsed with 100 µM 4-SU (Sigma) for 16–24 hr and crosslinked with 400 mJ/cm^2 UVA (365 nm) using a Stratalinker UV crosslinker (Stratagene). Cells were lysed for 10 min at 37°C in CLIP buffer (20 mM HEPES [pH 7.4], 5 mM EDTA, 150 mM NaCl, 2% lauryldimethylbetaine) with protease inhibitors, 20 U/ml Turbo DNase (Life Technologies), and 200 U/ml murine RNase inhibitor (New England Biolabs). IPs were carried out in CLIP buffer for 1 hr at 4°C. When necessary, extracts were treated with RNase A + T1 cocktail (Ambion) for 5′ at 37°C. Immunocomplexes were recovered with protein G-coupled dynabeads for 45 min at 4°C. DNA was removed with Turbo DNase (2 U in 20 µl). Crosslinked RNA was labeled by incubations with 5U Antarctic phosphatase and 5U T4 PNK (both from New England Biolabs) in presence of 10 µCi [γ-^{32}P] ATP (PerkinElmer, MA). Labeled material was resolved on 8% bis-tris gels, transferred to nitrocellulose, and exposed to autoradiography films for 1–24 hr.

For PAR-CLIP-seq, 100 pmol of a 3′-blocked DNA adaptor was ligated to the RNA after dephosphorylation and before 5′ labeling by incubating the beads with T4 RNA ligase 1 (New England Biolabs) for 1 hr at 25°C. After autoradiography, bands were excised and the RNA eluted with proteinase K for 30 minutes at 37°C and proteinase K in 3.5M urea for 30 minutes at 55°C. Custom 5′ adapters were ligated, and the products were size-selected on polyacrylamide or agarose gels, amplified, and sequenced on an Illumina HiSeq 2000.

For the analysis, adapter sequences were removed and reads < 17 nt discarded. The remaining reads were mapped to the mm9 genome using BOWTIE (Langmead et al., 2009), allowing two mismatches and removing duplicates. RCSs were identified with PARalyzer (Corcoran et al., 2011) requiring at least two T→C conversions per RCS. For Figure 2F, RCSs were assigned to lncRNAs in ENSEMBL 67 when they overlapped anywhere within the gene body to account for imprecisions in the annotation of lncRNAs.

RNA Structural Predictions

Structural predictions and minimum free-energy calculations shown in Figure S3 were performed with the Vienna RNA Websuite using default settings (Gruber et al., 2008).

ACCESSION NUMBERS

The ChIP and CLIP sequences reported in this paper have been deposited to the Gene Expression Omnibus (GEO) with the accession number GSE48518. EZH2 PAR-CLIP-seq data used for comparative analyses were taken from GEO accession number GSE49433 (Kaneko et al., 2013).

SUPPLEMENTAL INFORMATION

Supplemental Information includes Supplemental Experimental Procedures, seven figures, and seven tables and can be found with this article online at http://dx.doi.org/10.1016/j.molcel.2013.11.012.

ACKNOWLEDGMENTS

We thank the Genome Technology Center at NYU for help with sequencing, John Rinn and Matthias Stadtfeld for comments on the manuscript, and Varun Narendra for bioinformatic analyses. This work was supported by grants from the National Institutes of Health (GM-64844 and R37-37120) and the Howard Hughes Medical Institute (to D.R.). R.B. was supported by a Helen Hay Whitney Foundation postdoctoral fellowship and by the Helen L. and Martin S. Kimmel Center for Stem Cell Biology postdoctoral fellow award. R.S.M. was supported by a Ph.D. and an international research stay fellowship from CONACyT (213029).

Received: July 10, 2013
Revised: October 2, 2013
Accepted: November 21, 2013
Published: December 26, 2013

REFERENCES

Benson, D.A., Karsch-Mizrachi, I., Lipman, D.J., Ostell, J., and Wheeler, D.L. (2004). GenBank: update. Nucleic Acids Res. *32* (Database issue), D23–D26.

Bonasio, R., Tu, S., and Reinberg, D. (2010). Molecular signals of epigenetic states. Science *330*, 612–616.

Boulay, G., Dubuissez, M., Van Rechem, C., Forget, A., Helin, K., Ayrault, O., and Leprince, D. (2012). Hypermethylated in cancer 1 (HIC1) recruits polycomb repressive complex 2 (PRC2) to a subset of its target genes through interaction with human polycomb-like (hPCL) proteins. J. Biol. Chem. *287*, 10509–10524.

Brockdorff, N., Ashworth, A., Kay, G.F., McCabe, V.M., Norris, D.P., Cooper, P.J., Swift, S., and Rastan, S. (1992). The product of the mouse Xist gene is a 15 kb inactive X-specific transcript containing no conserved ORF and located in the nucleus. Cell *71*, 515–526.

Brown, C.J., Hendrich, B.D., Rupert, J.L., Lafrenière, R.G., Xing, Y., Lawrence, J., and Willard, H.F. (1992). The human XIST gene: analysis of a 17 kb inactive X-specific RNA that contains conserved repeats and is highly localized within the nucleus. Cell *71*, 527–542.

Corcoran, D.L., Georgiev, S., Mukherjee, N., Gottwein, E., Skalsky, R.L., Keene, J.D., and Ohler, U. (2011). PARalyzer: definition of RNA binding sites from PAR-CLIP short-read sequence data. Genome Biol. *12*, R79.

da Rocha, S.T., Edwards, C.A., Ito, M., Ogata, T., and Ferguson-Smith, A.C. (2008). Genomic imprinting at the mammalian Dlk1-Dio3 domain. Trends Genet. *24*, 306–316.

Davidovich, C., Zheng, L., Goodrich, K.J., and Cech, T.R. (2013). Promiscuous RNA binding by Polycomb repressive complex 2. Nat. Struct. Mol. Biol. *20*, 1250–1257.

Dignam, J.D., Lebovitz, R.M., and Roeder, R.G. (1983). Accurate transcription initiation by RNA polymerase II in a soluble extract from isolated mammalian nuclei. Nucleic Acids Res. *11*, 1475–1489.

Gao, Z., Zhang, J., Bonasio, R., Strino, F., Sawai, A., Parisi, F., Kluger, Y., and Reinberg, D. (2012). PCGF homologs, CBX proteins, and RYBP define functionally distinct PRC1 family complexes. Mol. Cell *45*, 344–356.

Ginis, I., Luo, Y., Miura, T., Thies, S., Brandenberger, R., Gerecht-Nir, S., Amit, M., Hoke, A., Carpenter, M.K., Itskovitz-Eldor, J., and Rao, M.S. (2004). Differences between human and mouse embryonic stem cells. Dev. Biol. *269*, 360–380.

Gruber, A.R., Lorenz, R., Bernhart, S.H., Neuböck, R., and Hofacker, I.L. (2008). The Vienna RNA websuite. Nucleic Acids Res. *36* (Web Server issue), W70–W74.

Guttman, M., Amit, I., Garber, M., French, C., Lin, M.F., Feldser, D., Huarte, M., Zuk, O., Carey, B.W., Cassady, J.P., et al. (2009). Chromatin signature reveals over a thousand highly conserved large non-coding RNAs in mammals. Nature *458*, 223–227.

Hafner, M., Landthaler, M., Burger, L., Khorshid, M., Hausser, J., Berninger, P., Rothballer, A., Ascano, M., Jr., Jungkamp, A.C., Munschauer, M., et al. (2010). Transcriptome-wide identification of RNA-binding protein and microRNA target sites by PAR-CLIP. Cell *141*, 129–141.

Hochedlinger, K., Yamada, Y., Beard, C., and Jaenisch, R. (2005). Ectopic expression of Oct-4 blocks progenitor-cell differentiation and causes dysplasia in epithelial tissues. Cell *121*, 465–477.

John, R.M., and Surani, M.A. (1996). Imprinted genes and regulation of gene expression by epigenetic inheritance. Curr. Opin. Cell Biol. *8*, 348–353.

Kagami, M., Sekita, Y., Nishimura, G., Irie, M., Kato, F., Okada, M., Yamamori, S., Kishimoto, H., Nakayama, M., Tanaka, Y., et al. (2008). Deletions and epimutations affecting the human 14q32.2 imprinted region in individuals with paternal and maternal upd(14)-like phenotypes. Nat. Genet. *40*, 237–242.

Kaneko, S., Rozenblatt-Rosen, O., Meyerson, M., and Manley, J.L. (2007). The multifunctional protein p54nrb/PSF recruits the exonuclease XRN2 to facilitate pre-mRNA 3′ processing and transcription termination. Genes Dev. *21*, 1779–1789.

Kaneko, S., Li, G., Son, J., Xu, C.F., Margueron, R., Neubert, T.A., and Reinberg, D. (2010). Phosphorylation of the PRC2 component Ezh2 is cell cycle-regulated and up-regulates its binding to ncRNA. Genes Dev. *24*, 2615–2620.

Kaneko, S., Son, J., Shen, S.S., Reinberg, D., and Bonasio, R. (2013). PRC2 binds active promoters and contacts nascent RNAs in embryonic stem cells. Nat. Struct. Mol. Biol. *20*, 1258–1264.

Kanhere, A., Viiri, K., Araújo, C.C., Rasaiyaah, J., Bouwman, R.D., Whyte, W.A., Pereira, C.F., Brookes, E., Walker, K., Bell, G.W., et al. (2010). Short RNAs are transcribed from repressed polycomb target genes and interact with polycomb repressive complex-2. Mol. Cell *38*, 675–688.

Khalil, A.M., Guttman, M., Huarte, M., Garber, M., Raj, A., Rivea Morales, D., Thomas, K., Presser, A., Bernstein, B.E., van Oudenaarden, A., et al. (2009). Many human large intergenic noncoding RNAs associate with chromatin-modifying complexes and affect gene expression. Proc. Natl. Acad. Sci. USA *106*, 11667–11672.

Kim, T.G., Kraus, J.C., Chen, J., and Lee, Y. (2003). JUMONJI, a critical factor for cardiac development, functions as a transcriptional repressor. J. Biol. Chem. *278*, 42247–42255.

Kim, H., Kang, K., and Kim, J. (2009). AEBP2 as a potential targeting protein for Polycomb Repression Complex PRC2. Nucleic Acids Res. *37*, 2940–2950.

Landeira, D., Sauer, S., Poot, R., Dvorkina, M., Mazzarella, L., Jørgensen, H.F., Pereira, C.F., Leleu, M., Piccolo, F.M., Spivakov, M., et al. (2010). Jarid2 is a PRC2 component in embryonic stem cells required for multi-lineage differentiation and recruitment of PRC1 and RNA Polymerase II to developmental regulators. Nat. Cell Biol. *12*, 618–624.

Langmead, B., Trapnell, C., Pop, M., and Salzberg, S.L. (2009). Ultrafast and memory-efficient alignment of short DNA sequences to the human genome. Genome Biol. *10*, R25.

Lanzuolo, C., and Orlando, V. (2012). Memories from the polycomb group proteins. Annu. Rev. Genet. *46*, 561–589.

Li, G., Margueron, R., Ku, M., Chambon, P., Bernstein, B.E., and Reinberg, D. (2010). Jarid2 and PRC2, partners in regulating gene expression. Genes Dev. *24*, 368–380.

Margueron, R., and Reinberg, D. (2011). The Polycomb complex PRC2 and its mark in life. Nature *469*, 343–349.

Margueron, R., Justin, N., Ohno, K., Sharpe, M.L., Son, J., Drury, W.J., 3rd, Voigt, P., Martin, S.R., Taylor, W.R., De Marco, V., et al. (2009). Role of the polycomb protein EED in the propagation of repressive histone marks. Nature *461*, 762–767.

Nishino, K., Toyoda, M., Yamazaki-Inoue, M., Fukawatase, Y., Chikazawa, E., Sakaguchi, H., Akutsu, H., and Umezawa, A. (2011). DNA methylation dynamics in human induced pluripotent stem cells over time. PLoS Genet. *7*, e1002085.

Pasini, D., Cloos, P.A., Walfridsson, J., Olsson, L., Bukowski, J.P., Johansen, J.V., Bak, M., Tommerup, N., Rappsilber, J., and Helin, K. (2010). JARID2 regulates binding of the Polycomb repressive complex 2 to target genes in ES cells. Nature *464*, 306–310.

Peng, J.C., Valouev, A., Swigut, T., Zhang, J., Zhao, Y., Sidow, A., and Wysocka, J. (2009). Jarid2/Jumonji coordinates control of PRC2 enzymatic activity and target gene occupancy in pluripotent cells. Cell *139*, 1290–1302.

Puda, A., Milosevic, J.D., Berg, T., Klampfl, T., Harutyunyan, A.S., Gisslinger, B., Rumi, E., Pietra, D., Malcovati, L., Elena, C., et al. (2012). Frequent deletions of JARID2 in leukemic transformation of chronic myeloid malignancies. Am. J. Hematol. *87*, 245–250.

Rinn, J.L., and Chang, H.Y. (2012). Genome regulation by long noncoding RNAs. Annu. Rev. Biochem. *81*, 145–166.

Rinn, J.L., Kertesz, M., Wang, J.K., Squazzo, S.L., Xu, X., Brugmann, S.A., Goodnough, L.H., Helms, J.A., Farnham, P.J., Segal, E., and Chang, H.Y. (2007). Functional demarcation of active and silent chromatin domains in human HOX loci by noncoding RNAs. Cell *129*, 1311–1323.

Schwartz, Y.B., and Pirrotta, V. (2007). Polycomb silencing mechanisms and the management of genomic programmes. Nat. Rev. Genet. *8*, 9–22.

Shen, X., Kim, W., Fujiwara, Y., Simon, M.D., Liu, Y., Mysliwiec, M.R., Yuan, G.-C., Lee, Y., and Orkin, S.H. (2009). Jumonji modulates polycomb activity and self-renewal versus differentiation of stem cells. Cell *139*, 1303–1314.

Son, J., Shen, S.S., Margueron, R., and Reinberg, D. (2013). Nucleosome binding activities within JARID2 and EZH1 regulate the function of PRC2 on chromatin. Genes Dev., in press. Published online December 15, 2013. gad.225888.113.

Stadtfeld, M., Apostolou, E., Akutsu, H., Fukuda, A., Follett, P., Natesan, S., Kono, T., Shioda, T., and Hochedlinger, K. (2010). Aberrant silencing of imprinted genes on chromosome 12qF1 in mouse induced pluripotent stem cells. Nature *465*, 175–181.

Takahashi, N., Okamoto, A., Kobayashi, R., Shirai, M., Obata, Y., Ogawa, H., Sotomaru, Y., and Kono, T. (2009). Deletion of Gtl2, imprinted non-coding RNA, with its differentially methylated region induces lethal parent-origin-dependent defects in mice. Hum. Mol. Genet. *18*, 1879–1888.

Takeuchi, T., Yamazaki, Y., Katoh-Fukui, Y., Tsuchiya, R., Kondo, S., Motoyama, J., and Higashinakagawa, T. (1995). Gene trap capture of a novel mouse gene, jumonji, required for neural tube formation. Genes Dev. *9*, 1211–1222.

Trojer, P., and Reinberg, D. (2007). Facultative heterochromatin: is there a distinctive molecular signature? Mol. Cell *28*, 1–13.

Tsai, M.C., Manor, O., Wan, Y., Mosammaparast, N., Wang, J.K., Lan, F., Shi, Y., Segal, E., and Chang, H.Y. (2010). Long noncoding RNA as modular scaffold of histone modification complexes. Science *329*, 689–693.

Ulitsky, I., Shkumatava, A., Jan, C.H., Sive, H., and Bartel, D.P. (2011). Conserved function of lincRNAs in vertebrate embryonic development despite rapid sequence evolution. Cell *147*, 1537–1550.

Wang, K.C., Yang, Y.W., Liu, B., Sanyal, A., Corces-Zimmerman, R., Chen, Y., Lajoie, B.R., Protacio, A., Flynn, R.A., Gupta, R.A., et al. (2011). A long noncoding RNA maintains active chromatin to coordinate homeotic gene expression. Nature *472*, 120–124.

Yap, K.L., Li, S., Muñoz-Cabello, A.M., Raguz, S., Zeng, L., Mujtaba, S., Gil, J., Walsh, M.J., and Zhou, M.M. (2010). Molecular interplay of the noncoding RNA ANRIL and methylated histone H3 lysine 27 by polycomb CBX7 in transcriptional silencing of INK4a. Mol. Cell *38*, 662–674.

Zhang, Y., Liu, T., Meyer, C.A., Eeckhoute, J., Johnson, D.S., Bernstein, B.E., Nusbaum, C., Myers, R.M., Brown, M., Li, W., and Liu, X.S. (2008). Model-based analysis of ChIP-Seq (MACS). Genome Biol. *9*, R137.

Zhao, J., Ohsumi, T.K., Kung, J.T., Ogawa, Y., Grau, D.J., Sarma, K., Song, J.J., Kingston, R.E., Borowsky, M., and Lee, J.T. (2010). Genome-wide identification of polycomb-associated RNAs by RIP-seq. Mol. Cell *40*, 939–953.

A synthetic nanofibrillar matrix promotes *in vitro* hepatic differentiation of embryonic stem cells and induced pluripotent stem cells

Taiji Yamazoe[1,2,3], Nobuaki Shiraki[1], Masashi Toyoda[4], Nobutaka Kiyokawa[4], Hajime Okita[4], Yoshitaka Miyagawa[4], Hidenori Akutsu[4], Akihiro Umezawa[4], Yutaka Sasaki[2], Kazuhiko Kume[1] and Shoen Kume[1,3,5,*]

[1]Division of Stem Cell Biology, Institute of Molecular Embryology and Genetics, Kumamoto University, Honjo 2-2-1, Kumamoto 860-0811, Japan
[2]Department of Gastroenterology and Hepatology, Faculty of Life Science, Kumamoto University, Honjo 2-2-1, Kumamoto 860-0811, Japan
[3]G.COE, Kumamoto University, Honjo 2-2-1, Kumamoto 860-0811, Japan
[4]Department of Reproductive Biology, National Institute for Child Health and Development, Okura 2-10-1, Setagaya, Tokyo 157-8535, Japan
[5]Program for Leading Graduate Schools 'HIGO (Health life science; Interdisciplinary and Glocal Oriented) Program', Kumamoto University, Honjo 221, Chuoku, Kumamoto 8600811, Japan
*Author for correspondence (skume@kumamoto-u.ac.jp)

Accepted 9 September 2013
Journal of Cell Science 126, 5391–5399

doi: 10.1242/jcs.129767

Summary

Embryonic stem (ES) cells recapitulate normal developmental processes and serve as an attractive source for routine access to a large number of cells for research and therapies. We previously reported that ES cells cultured on M15 cells, or a synthesized basement membrane (sBM) substratum, efficiently differentiated into an endodermal fate and subsequently adopted fates of various digestive organs, such as the pancreas and liver. Here, we established a novel hepatic differentiation procedure using the synthetic nanofiber (sNF) as a cell culture scaffold. We first compared endoderm induction and hepatic differentiation between murine ES cells grown on sNF and several other substrata. The functional assays for hepatocytes reveal that the ES cells grown on sNF were directed into hepatic differentiation. To clarify the mechanisms for the promotion of ES cell differentiation in the sNF system, we focused on the function of Rac1, which is a Rho family member protein known to regulate the actin cytoskeleton. We observed the activation of Rac1 in undifferentiated and differentiated ES cells cultured on sNF plates, but not in those cultured on normal plastic plates. We also show that inhibition of Rac1 blocked the potentiating effects of sNF on endoderm and hepatic differentiation throughout the whole differentiation stages. Taken together, our results suggest that morphological changes result in cellular differentiation controlled by Rac1 activation, and that motility is not only the consequence, but is also able to trigger differentiation. In conclusion, we believe that sNF is a promising material that might contribute to tissue engineering and drug delivery.

Key words: Hepatic differentiation, *In vitro* differentiation, Embryonic stem cells, Induced pluripotent stem cells

Introduction

The liver is an important organ that performs many complex functions, including the metabolism of carbohydrates, proteins and lipids, as well as storage of essential nutrients and biotransformation of drugs. Drug biotransformation involves detoxification and bioactivation, where the metabolite becomes more toxic. Therefore, drug biotransformation plays an important role in the early stages of drug discovery processes. Primary hepatocyte cultures are often used for pharmacological assays, but they are short-lived and cannot be maintained in long-term culture. In addition, there are considerable donor-dependent variations. By contrast, embryonic stem (ES) cells or induced pluripotent stem (iPS) cells can proliferate infinitely and maintain their pluripotent ability to differentiate into various cell types. There is evidence that ES or iPS cells recapitulate normal developmental processes, and can serve as an alternative resource for hepatological researches, drug development and clinical uses. Through our present knowledge of developmental biology, efficient induction of hepatic lineage cells has been established. For example, based on the evidence that TGFβ–activin–Smad2 signaling is involved in definitive endoderm formation in the mouse (Tremblay et al., 2000), the activation of Activin–Nodal signaling was used for endoderm induction (D'Amour et al., 2005; Kubo et al., 2004). Fibroblast growth factor (FGF) and bone morphogenetic protein (BMP) were added for the specification of liver lineages (Jung, 1999; Mfopou et al., 2010; Shiraki et al., 2008a); this helped to mimic the mesodermal signals from the septum transversum mesenchyme in normal development (Katsumoto et al., 2010; Shin et al., 2007; Rossi et al., 2001). Because hepatocyte growth factors are known to be important effectors in the specification of cell fate and organogenesis of the liver (Schmidt et al., 1995; Sonnenberg et al., 1993), hepatocyte growth factor (HGF), dexamethasone and oncostatin M have been used for induction of hepatocyte maturation (Basma et al., 2009; Kamiya et al., 1999; Si-Tayeb et al., 2010). Compared with the factors described above that direct hepatic differentiation, the role of extracellular matrices (ECMs) and scaffolds remains unclear.

We have previously reported that culturing ES/iPS cells on the mesonephric M15 cell line, in the presence of specific growth factors, resulted in an efficient induction of endoderm-derived tissues, such as the liver or pancreas (Shiraki et al., 2008a; Shiraki et al., 2008b; Umeda et al., 2013). We further suggested that the basement membrane components, including *lama5*, play an important role in guiding the differentiation of ES cells into regional-specific lineages of the definitive endoderm (Higuchi et al., 2010). We also successfully established an alternative hepatic differentiation procedure without using feeder cells, but with a synthesized basement membrane (sBM) substratum (Higuchi et al., 2010; Shiraki et al., 2011). Together, these results revealed the importance of the ECM for differentiation of ES cells.

The basement membrane, a highly integrated three-dimensional structure composed of ECM molecules, is known to regulate various cellular processes. It is known that electrospun nanofibers provide not only three-dimensional microenvironments mimicking the ECM, but also appropriate guidance cues to modulate cell behavior. Here, we tested the effects of synthetic nanofiber (sNF) matrices on ES/iPS cell differentiation. We found that ES/iPS cells grown on the sNF were induced into endoderm and then hepatic fates. Overall, we conclude that the sNF is more potent in promoting hepatic differentiation, compared with the traditional two-dimensional culture surfaces, and is able to substitute for the sBM or M15 cells.

Results

Differentiation of murine and human ES cells into the hepatic lineages on the sNF matrix

We first tested the sNF matrix for its potency to mimic the basement membrane substratum of the cells. Murine SK7 ES cells (Shiraki et al., 2008a) were seeded onto the sNF matrix, and allowed to differentiate into the hepatic lineage by sequential changes of medium containing specific growth factors (Fig. 1A). We found that the expression of the pluripotent marker *Oct3/4* was downregulated, whereas the mesendoderm marker *Gsc* and definitive endoderm markers *Sox17* and *Foxa2* were expressed at day 4 (d4) of differentiation (Fig. 1B). Whereas *Gsc* was downregulated rapidly, *Sox17* and *Foxa2* showed peak expressions around d7 and were downregulated afterwards. Notably, the hepatic progenitor marker gene, alpha-fetoprotein (*Afp*), and the mature hepatocyte marker, albumin (*Alb1*) were detectable from d12 and d16, respectively, and their expression levels were increased with time. Although the *Afp* transcript level was decreased after d22, the *Alb1* expression continued increasing beyond d22. The immunocytochemical analysis further confirms that ALB and AFP were present in the cytoplasm of differentiated ES cells (Fig. 1C). In addition, periodic-acid–Schiff (PAS) staining and the Indocyanin Green (ICG) test were also conducted to investigate the hepatocyte functions of differentiated ES cells. The former reflects glycogen storage by showing positive populations as magenta in the cytoplasm, and the latter is used to examine cellular uptake activities, which are regarded as a hepatocyte detoxification function. As shown in Fig. 1D, glycogen storage was observed as the accumulation of magenta staining in the cytoplasm of the differentiated cells (top panel) and the ICG test also shows a similar result (bottom panel).

We next investigated whether human ES or iPS cells could differentiate in the sNF system. We used khES3 human ES cells

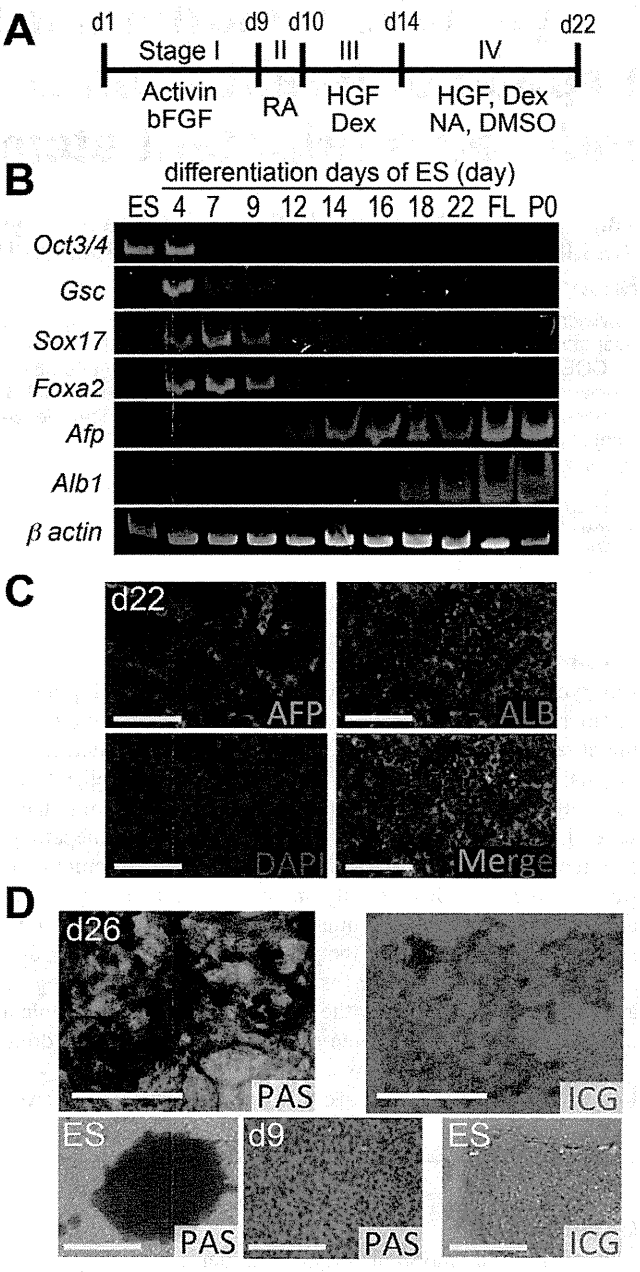

Fig. 1. Differentiation of murine ES cells into the hepatocyte lineage on nanofiber scaffolds. (A) Schematic diagram of the differentiation procedure for mouse ES cells. (B) Time-dependent expression levels of endoderm and hepatic marker genes. β-actin was used as a control. FL, fetal liver on embryonic day 12.5; P0, neonatal liver on postnatal day 0. (C) The immunochemical analysis of differentiated ES cells on day 22 (d22) for α-fetoprotein (AFP, green) and albumin (ALB, red) with nuclear counterstaining (DAPI). (D) Hepatocyte functional tests for PAS and ICG on d26 differentiated ES cells (top panels) and undifferentiated (bottom left and right panels) and d9 differentiated (bottom middle panel) ES cells as negative controls (bottom panels). Nuclei are counterstained with hematoxylin (blue). Scale bars: 250 μm.

(supplementary material Fig. S1A–D), as well as human iPS cell lines, such as Toe (supplementary material Fig. S1E,G) and 201B7 (supplementary material Fig. S1F), and found that these cells were able to differentiate into hepatocyte-like cells, thereby

producing ALB and taking up ICG (supplementary material Fig. S1D–G). Together, these results indicate that sNF is a suitable matrix for potentiating hepatic differentiation, not only in murine cells, but also in human ES cells and iPS cells.

sNF is more potent than normal plates precoated with other matrices

To compare the supportive effects of NFs and other substrata, we seeded murine ES cells onto either the sNF matrix or normal plates precoated with other stubstrata, including collagen I, Matrigel, gelatin and fibronectin and then performed the differentiation experiment as described in Fig. 1A. On differentiation day 22 (d22), quantitative PCR analyses were carried out to quantify the expression profiles of hepatic function marker genes in differentiated cells. Our results indicate that ES cells grown on sNF showed higher expression levels of proteins secreted by hepatocytes, such as serine peptidase inhibitor a1 (*Serpina1*), *Ttr* and *Alb1*, compared with those grown on other substrata (Fig. 2). Similar results were observed for the expression of several other genes, including glucose 6-phosphatase (*G6p*) and fatty-acid

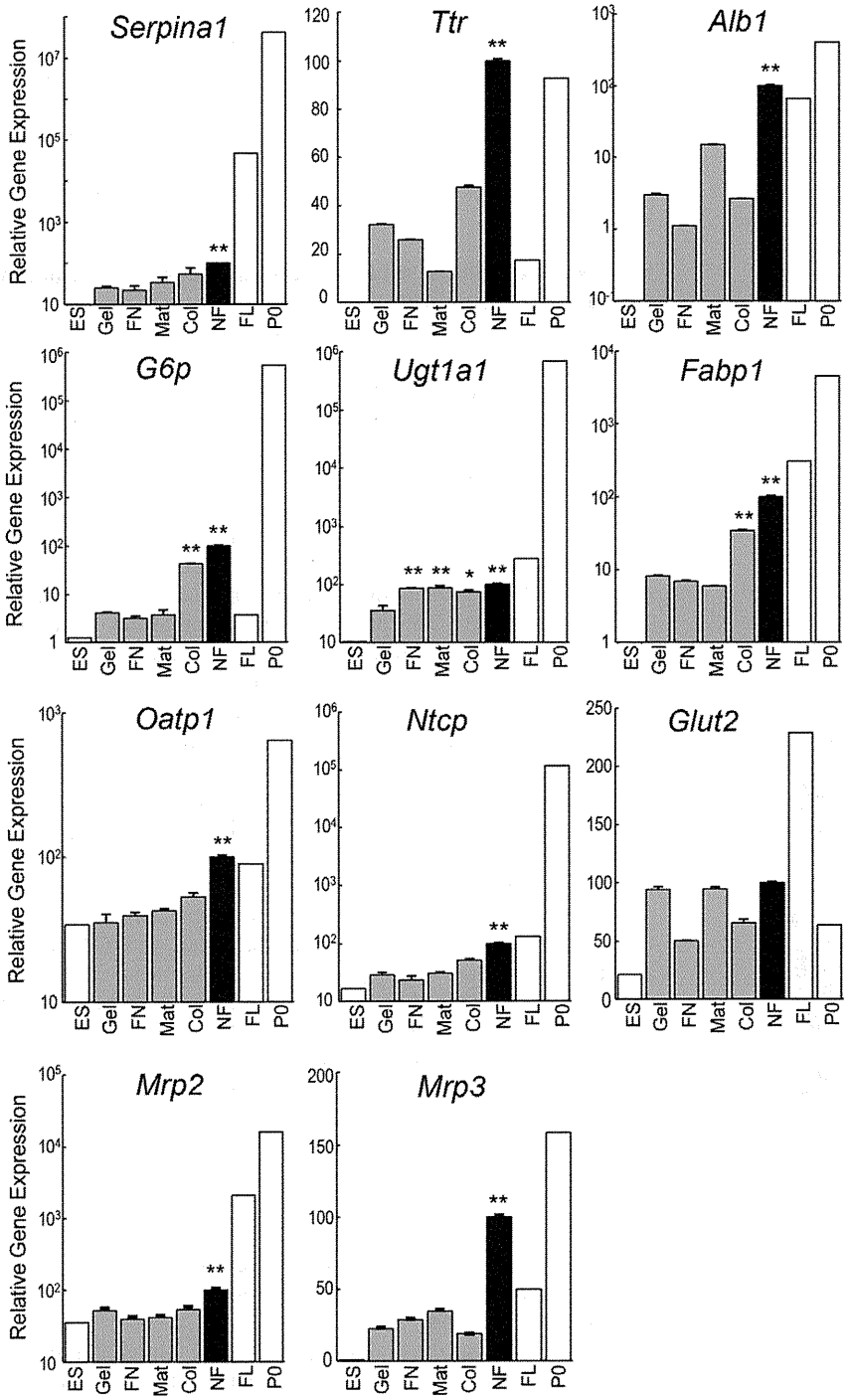

Fig. 2. Expression of hepatic markers in differentiated murine ES cells on sNF or other substrata. Expression levels of various gene transcripts quantified by real time PCR in d22 differentiated ES cells cultured on sNF, collagen I (Col), Matrigel (Mat), fibronectin (FN) or gelatin (Gel). ES, undifferentiated ES cells. FL (E12.5 fetal liver) and P0 (neonatal liver on postnatal day 0) are used as references. For differentiated ES cells, values represent mean ± s.e.m. (n=3). *P<0.05 and **P<0.01, by one-way ANOVA with the post-hoc Dunnett's test.

binding protein (*Fabp1*), or transporters, such as organic anion-transporting polypeptide 1 (*Oatp1*), Na^+-taurocholate cotransporting polypeptide (*Ntcp*) and UDP-glucuronosyltransferase (*Ugt1a1*), as well as multidrug resistance-associated protein family proteins 2 and 3 (*Mrp2* and *Mrp3*) (Fig. 2). By contrast, little change was found in the expression of glucose transporter 2 (*Glut2*).

To determine the hepatic functions of differentiated ES cells grown on Matrigel, collagen I or sNF, we next measured their ALB secretions, ICG uptake and cytochrome p450 (CYP) activities. Our results show that ES cells grown on sNF secreted ALB at a higher level compared with those on Matrigel or collagen I (Fig. 3A). By day 26, the percentage of ICG-positive ES cells on sNF was also higher than in ES cells grown on the other two substrates (Fig. 3B,C).

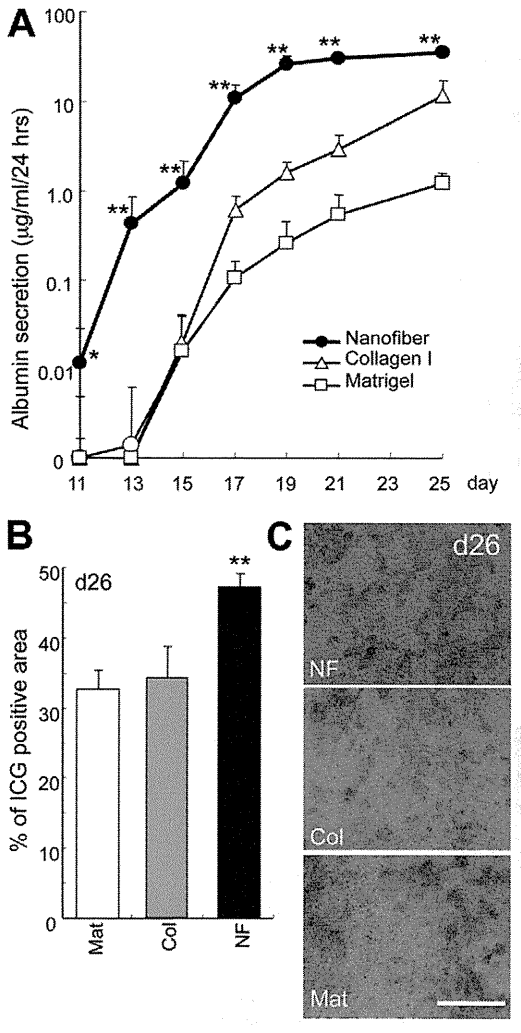

Fig. 3. Liver functional assays of differentiated murine ES cells grown on nanofiber scaffolds versus other substrata. (A) ELISA analysis of time-dependent albumin secretion for 24 hours by ES cells grown on Matrigel (Mat), collagen I (Col) or NF. (B,C) ICG tests performed on d26 differentiatied ES cells. The percentage of cells taking up ICG in culture was calculated (B) and representative images are shown (C). Values represent means ± s.e.m. (n=6). *P<0.05, **P<0.01, by two-tailed Student's t-test. Scale bar: 250 μm.

To measure CYP activities, the differentiated ES cells were treated with a CYP1A inducer, 3-methylcholantrene (3MC), for 48 hours during d22–d24 or d64–d66, as shown in supplementary material Fig. S2A. We found that the differentiated cells cultured on sNF had higher CYP1A1 activities and responses to the inducer than those cultured on fibronectin, Matrigel or collagen I (supplementary material Fig. S2B). We also assayed the effects of sNF on the maintenance of the mature hepatic cells. ES cells cultured on sNF were able to maintain their CYP1A1 activities and responses to 3MC even on d66, whereas those cultured on other matrices did not survive in long-term cultures (supplementary material Fig. S2C). It is also worth noting that the differentiated cells on sNF could be maintained in culture for more than 100 days. Specifically, we show that the ES cells cultured on sNF for 129 days were able to uptake and secrete ICG (supplementary material Fig. S2D). Based on these findings, we conclude that sNF is an excellent matrix, not only for the differentiation of ES cells into the hepatic lineage but also for maintaining the mature state of ES-cell-derived hepatocytes.

High Rac1 activities in undifferentiated and differentiated ES cells grown on sNF

Next, we investigated the effects of sNF on hepatic differentiation of ES cells. It was previously reported that the undifferentiated murine ES cells cultured on sNF exhibited spheroid morphologies and formed dome-like structures, and proliferated well (Nur-E-Kamal et al., 2006). Therefore, we checked the morphological changes between the undifferentiated and differentiated states of the murine ES cells. To exclude the effect of the extracellular matrix, we compared gelatin-coated normal two-dimensional (2D) plates with either gelatin-coated or uncoated sNF. We found that the undifferentiated ES cells grown on gelatin-coated 2D plates, with cytoplasmic spreading morphologies and attached to the plate surface in large areas (Fig. 4A, left). By contrast, the ES cells grown on sNF showed aggregated morphologies (Fig. 4A, middle and right).

In the differentiated state, the ES cells were found to form a monolayer on sNF. However, the morphological differences were still observed between ES cells cultured on sNF or normal 2D plates (Fig. 4B). Because these morphological changes are known to be regulated by cytoskeletal molecules, such as small Rho GTPase family member proteins, we next examined Rac1 activities in undifferentiated and differentiated ES cells. Our western blot analyses demonstrate that the GTP-bound active form of Rac1 was expressed at a higher level in ES cells cultured on sNF than those cultured on normal 2D plates, even though total Rac1 expression levels were similar (Fig. 4C,D). Interestingly, both the undifferentiated (Fig. 4C) and the differentiated ES cells on d8 (Fig. 4D) showed higher Rac-GTP activities. These results not only agree with the morphological differences of the ES cells, but also suggest that activated Rac1 plays a crucial role in potentiating the differentiation activity of ES cells cultured on sNF into hepatic lineages.

A crucial role of Rac activation in potentiating the differentiation of ES cells into the definitive endoderm and hepatocyte lineages

NSC23766 is a selective inhibitor of Rac1 activation that is mediated by the Rac-specific guanine nucleotide exchange factors (GEFs) TrioN and Tiam1, without affecting other Rho

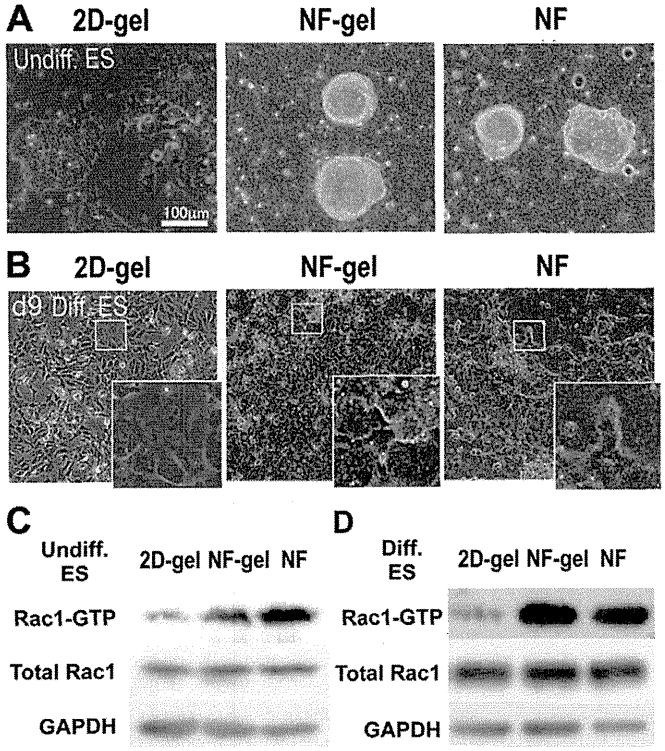

Fig. 4. NF induces Rac1 hydroxylation in both undifferentiated and day 9 differentiated murine ES cells. (A,B) Representative images of undifferentiated (A) and day 9 (d9) differentiated (B) ES cells grown on gelatin-precoated normal plates (2D-gel), gelatin-coated NF plates (NF-gel) and uncoated NF plates (NF). Insets are higher magnifications of the boxed regions. (C,D) Western blot analysis of GTP-bound active Rac1, total Rac1 and GAPDH expression in undifferentiated (C) or differentiated (D) ES cells described in A,B.

family members, such as RhoA or Cdc42 (Gao et al., 2004). We confirmed that 100 μM NSC23766 inhibited Rac1 hydroxylation (supplementary material Fig. 3A). To test whether sNF potentiates the differentiation of ES cells into the hepatic lineages through Rac1 activation, we treated murine ES cells with 100 μM NSC23766 at various stages and then determined the expression of stage-specific markers (Fig. 5A–C). We first added NSC23766 for 4 days at stage I to examine the effect of Rac1 activation on endoderm induction (Fig. 5A). We found that *Foxa2* expression was downregulated by the Rac1 inhibitor in ES cells cultured on sNF (Fig. 5A). We next examined the effects of Rac1 inhibition on hepatic differentiation. Our results show that the Rac1 inhibitor added at stage II (Fig. 5B) or stage III (Fig. 5C) downregulated the expression of hepatic markers, *Afp* or *Alb1*, on d10 or d14, respectively.

These results suggested that Rac1 activation is crucial for endoderm and hepatic differentiation. We subsequently examined the stage dependency of hepatic differentiation on Rac1 activities. The Rac1 inhibitor was added at different stages (I, II, III or IV) and *Alb1* expression was assayed on day 18 (Fig. 5D). We found that Rac1 inhibition at all four stages blocked the potentiating effects of sNF, and resulted in decreases in *Alb1* expression. These results further confirm the important role of Rac1 and demonstrate that continuous activation of Rac1 is crucial for the potentiation of hepatic differentiation.

Then we confirmed whether NSC23766 had any effect on the proliferation of ES cells. NSC23766 decreased the proportion of EdU-positive cells in stages I, II and III, particularly in stage I, without apparent toxicity (supplementary material Fig. S3C). Interestingly, the total numbers of cells in the NSC23766-treated groups was smaller in stages I and II, which became greater than that of control groups used in stages III and IV (supplementary material Fig. S3B). Taken together, these findings suggest that Rac1 differentially contributes to proliferation in the early differentiation stages and promotes differentiation in the late stage.

Discussion

Our previous study suggested that although addition of soluble growth factors is sufficient to promote the differentiation of ES cells into the definitive endoderm, further differentiation from the definitive endoderm into hepatic and pancreatic fates appears to require a direct contact with M15 cells (Shiraki et al., 2008a). We previously showed the importance of basement membrane substratum by culturing ES cells on sBM (Higuchi et al., 2010; Shiraki et al., 2011). Specifically, ES cells grown on sBM were able to differentiate into hepatic and pancreatic lineages. These results imply that the basement membrane structure plays a major role in the differentiation of ES cells. Although the sBM used previously was constructed by overexpressing recombinant laminin-511 (laminin α5, laminin β1 and laminin γ1) in H293 cells (Doi et al., 2002), ES cells or iPS cells could be induced into the hepatic and pancreatic lineages. The efficacy of such an sBM for differentiation was high, and the differentiated cells could perform liver-specific functions, such as protein secretion, detoxification and glycogen storage (Higuchi et al., 2010; Shiraki et al., 2011).

The nanofiber produced by the electrospinning technique is a chemically and physically stable synthetic three-dimensional surface that mimics the structural geometry and porosity of the basement membrane or ECM (Schindler et al., 2005; Schindler et al., 2006). NF scaffolds have been shown to recapitulate the structural features of stem cell niche (Lim and Mao, 2009) and have been used for the *ex vivo* expansion of various types of stem cells such as murine ES cells (Hashemi et al., 2011; Nur-E-Kamal et al., 2006) and human tissue stem cells. In addition, the ECM was found to deposit as an extensive scaffold on the basal surface of the cells attached to NFs (Shih et al., 2006; Chua et al., 2007; Ma et al., 2008). Importantly, the sNF system has been reported to enhance not only the differentiation of murine ES cells into neural lineages (Lim et al., 2010; Purcell et al., 2012; Xie et al., 2009), but also differentiation from human MSCs into hepatoblasts (Ghaedi et al., 2012; Kazemnejad et al., 2009).

Taken together, these previous observations revealed that the sNF matrix is useful as a substratum to replace feeder cells and that it has the ability to potentiate hepatic differentiation. In this study, we show that both murine and human ES cells, as well as human iPS cells, could differentiate on sNF and exhibit liver-specific functions. Furthermore, we demonstrate that Rac1 activation was involved in hepatic differentiation. Rac1, a member of the Rho family GTP-binding proteins, including Rho and Cdc42 (Heasman and Ridley, 2008), functions by activating actin-rich lamellipodial protrusion and membrane ruffling, which are thought to be a major part of the driving force for cell movement (Nobes and Hall, 1995; Ridley et al., 1992). Although Rho family proteins were reported to be

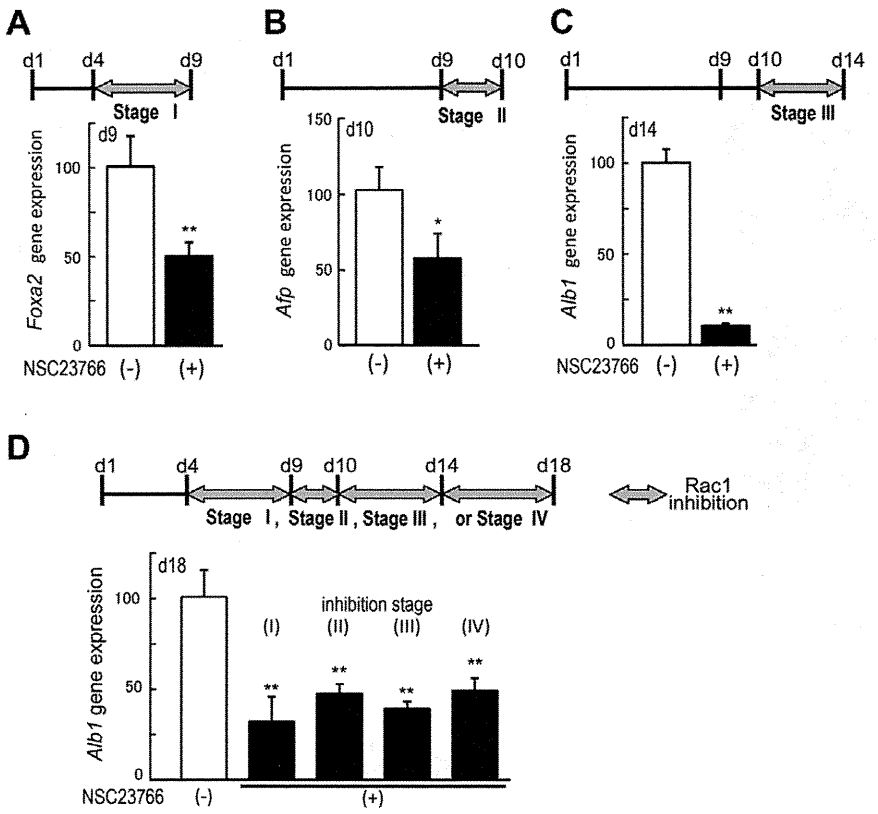

Fig. 5. Inhibition of the Rac1 pathway blocks the differentiation-potentiating activity of NF. (A–C) Quantitative PCR analysis of the gene expression of *Foxa2* (A), *Afp* (B) and *Alb1* (C), in differentiated cells cultured on sNF with (+) or without (−) the Rac1 inhibitor NSC23766 (100 μM), at the end of stage I (A), stage II (B) or stage III (C). (D) The expression of *Alb1* on day 18 in differentiated cells, treated with (+) or without (−) the Rac1 inhibitor at indicated stages. Data shown represent mean ± s.e.m. (n=3); *P<0.05 and **P<0.01, compared with untreated cells on sNF with the Rac1 inhibitor by two-tailed Student's t-test or one-way ANOVA with the post-hoc Dunnett's test.

expressed by ES cells cultured on sNF (Nur-E-Kamal et al., 2005; Nur-E-Kamal et al., 2006; Schindler et al., 2006), their roles have never been investigated.

In vivo developmental processes occurring in the endoderm and its derivatives cause dynamic migration during gastrulation and later stages of organogenesis (Woo et al., 2012), suggesting that motility and differentiation are closely inter-related. In this study, we observed that ES cells cultured on sNF showed greater Rac1 activation than did cells cultured on the normal 2D surface. Indeed, Rac1 is known to be involved in not only endoderm induction but also hepatic specification and maturation. In particular, *Rac1* mutant mice died by mouse embryonic day 9.5 (E9.5) because of severe developmental abnormalities, and *Rac1*-deficient embryos showed numerous cell deaths in the space between the ectoderm and endoderm at the primitive streak stage (Sugihara et al., 1998). Rac1 is also important for cellular differentiation, for example, epithelial differentiation in the small intestine (Stappenbeck and Gordon, 2000), pancreatic islet morphogenesis (Greiner et al., 2009), myogenic differentiation (Heller et al., 2001), maintenance of the thymic epithelial cells (Hunziker et al., 2011), formation of the lens (Maddala et al., 2011) and neuronal development (Corbetta et al., 2009; Leone et al., 2010). In addition, Rac1 has been shown to crosstalk with many downstream signaling pathways such as Wnt (Clarke, 2006; Malliri et al., 2006), TGF-β1 (Varon et al., 2008), Nodal (Woo et al., 2012), retinoic acid (Lee et al., 2008) and Myc (Hunziker et al., 2011; Nikolova et al., 2008). Interestingly, Rac1 is also known to mediate stem cell-shape-dependent regulation of differentiation to a chondrogenic versus myogenic fate (Gao et al., 2010). On the basis of these studies, we postulate that the sNF system might potentiate ES cells to differentiate into hepatic lineages by interacting downstream of certain growth factors during differentiation processes.

In conclusion, we show that Rac1 was activated in both undifferentiated and differentiated ES cells cultured on sNF plates and that Rac1 inhibition blocked the potentiating effects of sNF on endoderm and hepatic differentiation. These results suggest that continuous activation of Rac1 throughout the differentiation stage is crucial for potentiating differentiation. Our results also highlight the morphological changes during differentiation along the Rac1 pathway, which controls cellular morphology, motility and differentiation into the hepatic lineage. Here, we established a completely chemically defined method that requires no serum or no xenogenic substrata, thereby eliminating the risk of contamination with unknown factors. We believe that this novel method could be an attractive culture model for pharmacological research and research on stem cell biology and therapeutic strategies.

Materials and Methods

ES and iPS cell lines

The murine ES cell line, SK7 (Shiraki et al., 2008a) was maintained on mouse embryonic fibroblast (MEF) feeders in Glasgow minimum essential medium (Invitrogen, Glasgow, UK) supplemented with 1000 units/ml leukemia inhibitory factor (LIF; Chemicon, Temecula, CA), 15% knocked-out serum replacement (KSR; Invitrogen), 1% fetal bovine serum (FBS; Hyclone, Logan, UT), 100 μM nonessential amino acids (NEAA; Invitrogen), 2 mM L-glutamine (L-Gln; Invitrogen), 1 mM sodium pyruvate (Invitrogen), 50 units/ml penicillin and 50 μg/ml streptomycin (PS; Invitrogen) and 100 μM β-mercaptoethanol (β-ME; Sigma-Aldrich, St Louis, MO).

Human ES cells (KhES-3) (Suemori et al., 2006) were from Dr Norio Nakatsuji and Dr Hirofumi Suemori (Kyoto University, Kyoto, Japan). They were used in accordance with the human ES cell guidelines of the Japanese government. This human ES work was approved by Kumamoto University institutional review board. Human iPS 201B7 cells were a gift from Dr Yamanaka (Kyoto University, Kyoto, Japan). The human iPS Toe cell line was established by M. Toyoda and

colleagues (National Institute for Child Health and Development, Tokyo, Japan). Undifferentiated human ES and iPS cells were maintained as described previously (Shiraki et al., 2008b).

Culture plates

Synthetic nanofiber (sNF) matrices were purchased from Corning Coster (Ultra-Web Synthetic Polyamine Surface #3873XX1; Cambridge, MA). Plate surfaces were coated with electrospun polyamide nanofibers. sNF matrices consisted of two kinds of polyamide polymers, A $(C_{28}O_4N_4H_{47})_n$ and B $(C_{28}O_{4.4}N_4H_{47})_n$, which were crosslinked in the presence of an acid catalyst, and were 200–400 nm in diameter (average 280 nm). Pore sizes, similar to those of the cell basement membrane, were ~700 nm. For comparison, Corning 96-well plates were pretreated for 3 hours at 37℃ with 0.1% gelatin (Sigma-Aldrich), Matrigel (BD, Franklin Lakes, NJ) or CellStart (Invitrogen). Collagen I (Nitta Gelatin, Japan) was diluted with Dulbecco's modified Eagle's medium (DMEM; Invitrogen) at a concentration of 1 mg/ml and plate surfaces were treated for 15 minutes, then dried until use.

Differentiation of murine ES cells into hepatic lineages on sNF

Murine ES cells plated at a density of 1.5×10^4 cells/cm^2 in culture plates described above were grown for 8 days in DMEM containing 4,500 mg/l glucose, s NEAA, L-Gln, PS, β-ME, 10 mg/ml insulin, 5.5 mg/ml transferrin, 6.7 pg/ml selenium (Insulin-Transferrin-Selenium-G Supplement; ITS, Invitrogen), 0.25% AlbuMAX II (Invitrogen), 10 ng/ml recombinant human activin-A (R&D Systems, Minneapolis, MN), 5 ng/ml; recombinant human bFGF, and cultured for 8 days. On day 9 (d9), the medium was changed to RPMI-1640 (Invitrogen) containing 10^{-6} M retinoic acid (RA; Stemolecule all-trans retinoic acid; Stemgent, Cambridge, MA) and B27 supplement (Invitrogen). On d10, medium was switched to 2000 mg/l glucose DMEM (Invitrogen), 10% KSR, 10 ng/ml recombinant human hepatocyte growth factor (Peprotech, Rocky Hill, NJ) and 10 μM dexamethasone (Sigma-Aldrich), and cultured until d14. Next, 1 mM nicotinamide (NA; Sigma-Aldrich) and 1% dimethylsufoxide (DMSO; Sigma-Aldrich), were added to medium and KSR was removed. Medium was replaced every 2 days with fresh medium and growth factors.

Human ES/iPS cells were pretreated with the ROCK inhibitor Y27632 (Wako, Japan) 1 day before trypsinization. Cells were plated at a density of 3×10^5 cells/cm^2 on Matrigel-coated sNF matrices with Y27632. The following two procedures were subsequently used to induce hepatic differentiation of various human ES/iPS cells; simplified (two-step) protocol, KhES3 and 201B7 cells; or conventional (three-step) protocol, Toe cells. In the simplified protocol, medium used at first contained B27 and 100 ng/ml activin-A in RPMI-1640, which was then, switched to 10 ng/ml HGF, 10 μM dexamethasone, 0.5% DMSO, 0.5 mM NA. In the conventional protocol, medium used first was the same as that in the simplified protocol, followed by 1% DMSO and 20% KSR in knockout DMEM/F12 (Invitrogen) for 6 days and, then DMEM containing HGF, dexamethasone and 10% KSR. Finally, the above medium was added with 0.5 mM NA. Medium was replaced every 2 days with fresh medium and growth factors. KhES3 and 201B7 cells were induced hepatic differentiation with simplified protocol, and Toe cells were treated with conventional protocol.

Periodic-acid–Schiff's staining

For detection of glycogen storage in the differentiated cells, periodic-acid–Schiff's (PAS) staining kit (Muto Pure Chemicals, Tokyo, Japan) was used. Cells cultured for 9 and 26 days, and undifferentiated ES cells were fixed in 3.3% formalin for 10 minutes, and stained following the manufacturer's instructions, then nuclear counterstaining with hematoxylin (blue) was performed.

Albumin secretion assay

The culture medium was replaced with fresh medium every 2 days, and supernatants were collected 24 hours after replacing the medium. The mouse (human) albumin secreted in the supernatant was determined using a mouse (human) ELISA quantification kit (Bethyl, Montgomery, TX).

Indocyanine Green (ICG) test

Indocyanine Green (Daiichi-Sankyo Pharm., Japan) was diluted with the above culture medium to a final concentration of 1 mg/dl. The ICG test solution was added to the differentiated ES cells after the appropriate culture periods and undifferentiated ES cells were used as controls, and incubated at 37℃ for 30 minutes. Then, after three washes with phosphate-buffered saline (PBS), the cellular uptake of ICG was examined by microscopy. The percentage ICG-positive areas represent the proportion of ICG-positive area versus total cell area, which were determined using ImageJ software (US National Institutes of Health, Bethesda, MD).

CYP inductions

To check the inducibilities of cytochrome P450 activities in response to inducers, we used the P450-Glo CYP Assay Kit (Promega, Madison, WI). The differentiated ES cells were treated with 5 μM 3-methylcholantrene as inducers of CYP1A. The medium containing the inducers was changed every 24 hours. 48 hours after treatment, we changed the medium and used the appropriate luminogenic CYP substrates (Luciferine-CEE for CYP1A). The cells were incubated at 37℃ for 3 hours, and then the supernatants were mixed with equal amount of detection reagent, according to the manufacturer's instructions. The luminescence was measured using a GloMax 96 microplate luminometer (Promega), and luminometer settings were as in the manufacturer's instructions. Cell numbers were calculated using CellTiter-Glo luminescent cell viability assays (Promega) to normalize P450-Glo assay values to cell number.

Immunocytochemistry

After culture for the appropriate times, cells were fixed in 4% paraformaldehyde in PBS for 30 minutes at room temperature. After removal of paraformaldehyde solution, the fixed cells were permeabilized with 0.1% Triton X-100 for 10 minutes. The permeabilized cells were rinsed several times with PBS and were then incubated with 20% Blocking One (Nacalai Tesque, Japan) in PBST (0.1% Tween-20 in PBS) for blocking. After blocking, the cells were incubated with the diluted antibody in 20% Blocking One in PBST (0.1% Tween-20 in PBS) in a humidified chamber overnight at 4℃. After washing the cells in PBST, cells were incubated with the secondary antibody in 20% Blocking One for 2 hours at room temperature in the dark. After washing off the secondary antibody in PBST, cells were counterstained with 6-diamidino-2-phenylindole (DAPI) (Roche Diagnostics, Switzerland). The following antibodies were used as primary antibodies: rabbit anti-alphafeto protein (Dako, Denmark), goat anti-albumin (Sigma-Aldrich), goat anti-Sox17, mouse anti-FoxA2 (R&D systems); secondary antibodies used were conjugated to Alexa Fluor 568, Alexa Fluor 488 and Alexa Fluor 633 (Invitrogen). For human ES cell cultures, goat antibodies against human albumin (Bethyl) were used as primary antibodies.

Cell proliferation assay

Cell proliferation was evaluated using Click-iT EdU assay kit (invitrogen). The cells cultured with or without NSC23766 were exposed to 10 μM of 5-ethnyl-2′-deoxyuridine (EdU) for 1 hour at 37℃ before fixation. The fixed cells were processed for immunocytochemistry as described above, with an additional step for EdU detection. Before incubation with secondary antibodies, the cells were incubated with EdU in the Click-iT reaction cocktail and Alexa Fluor 488 for 30 minutes at room temperature, following the manufacturer's instructions. Images were collected using ImageXpress Micro (Molecular Devices) and EdU-positive nuclei per total number of nuclei were counted.

RT-PCR analysis

RNA was extracted from ES cells or mouse liver using an RNeasy mini-kit (Qiagen, Germany) and then treated with DNase (Qiagen). For reverse transcription reactions, 3 μg RNA was reverse-transcribed using ReverTra Ace (Toyobo, Japan) and oligo dT primers (Toyobo). One μl of fivefold-diluted cDNA (1% of the RT product) was used for PCR analyses. The primer sequences for each primer set are shown in supplementary material Table S1. For real-time PCR analysis, mRNA expression was quantified with SyberGreen on an ABI 7500 thermal cycler (Applied Biosystems, Foster City, CA). The PCR conditions were as follows: denaturation at 95℃ for 15 seconds, annealing and extention at 60℃ for 60 seconds, for up to 40 cycles. Each measurement was normalized to β-actin (mouse) and *GAPDH* (human) for each sample by subtracting the average β-actin (mouse) and *GAPDH* (human) C_t values (Threshold Cycle) from the average C_t for each gene. Target mRNA levels, expressed as arbitrary units, were determined using a standard curve method.

Rac pull-down assay

Murine ES cells were trypsinized and suspended at a density of 5×10^4 cells/ml. Cells were then plated onto sNF either with or without 0.1% gelatin pretreatment; control plates were pretreated with 0.1% gelatin. Undifferentiated cells were harvested 48 hours after incubation under ES cell maintenance culture conditions at 37℃, whereas differentiated cells were harvested 9 days after hepatic differentiation started. The activation of Rac was determined using a Rac1 Activation Assay Kit purchased from Millipore. Briefly, cells were washed with PBS and suspended in lysis buffer provided by the supplier. Aliquots were taken from each cell lysate, and the amount of GAPDH proteins present in the lysates was determined and used for normalization. GTP-bound forms of Rac were then pulled down from lysates using reagents provided by the supplier, following the recommended instructions. Proteins present in total cell lysates or Rac pull-down samples were separated by SDS-PAGE (12%) and transferred onto a nylon membrane. Western blotting was performed using antibodies against Rac1, according to the ECL protocol provided by the suppliers. Luminescence of Rac1 bands was quantified using the GE ImageQuant LAS 4000 (GE Healthcare Life Science, Sweden).

Acknowledgements

We thank members of Gene Technology Center in Kumamoto University for their technical assistance.

Author contributions

T.Y. performed cellular and biochemical analyses; T.Y. and N.S. established the ES cell differentiation system; M.T., N.K., H.O., Y.M., H.A. and A.U. established human iPS Toe cell line; Y.S., K.K. and S.K. provided technical advice, designed the experiments and wrote the paper. All authors discussed the results and commented on the manuscript.

Funding

This work was supported by a grant (to S.K.) from the Realization of Regenerative Medicine from the Ministry of Education, Culture, Sports, Science and Technology (MEXT) Japan; a grant from National Institute of Biomedical Innovation (to N.S.); a funding program for Next Generation World-Leading Researchers (NEXT Program) from the Japan Society for the Promotion of Science (JSPS) [grant number LS099 to S.K.] (to S.K.); and the Program for Leading Graduate Schools "HIGO" (to S.K.) a global COE grant (Cell Fate Regulation Research and Education Unit) from MEXT. S.K. was a member of Program (Cell Fate Regulation Research and Education Unit), MEXT, Japan.

Supplementary material available online at
http://jcs.biologists.org/lookup/suppl/doi:10.1242/jcs.129767/-/DC1

References

Basma, H., Soto-Gutiérrez, A., Yannam, G. R., Liu, L., Ito, R., Yamamoto, T., Ellis, E., Carson, S. D., Sato, S., Chen, Y. et al. (2009). Differentiation and transplantation of human embryonic stem cell-derived hepatocytes. *Gastroenterology* **136**, 990-999.

Chua, K.-N., Chai, C., Lee, P.-C., Ramakrishna, S., Leong, K. W. and Mao, H.-Q. (2007). Functional nanofiber scaffolds with different spacers modulate adhesion and expansion of cryopreserved umbilical cord blood hematopoietic stem/progenitor cells. *Exp. Hematol.* **35**, 771-781.

Clarke, R. (2006). Wnt signalling in the mouse intestine. *Oncogene* **25**, 7512-7521.

Corbetta, S., Gualdoni, S., Ciceri, G., Monari, M., Zuccaro, E., Tybulewicz, V. L. J. and de Curtis, I. (2009). Essential role of Rac1 and Rac3 GTPases in neuronal development. *FASEB J.* **23**, 1347-1357.

D'Amour, K. A., Agulnick, A. D., Eliazer, S., Kelly, O. G., Kroon, E. and Baetge, E. E. (2005). Efficient differentiation of human embryonic stem cells to definitive endoderm. *Nat. Biotechnol.* **23**, 1534-1541.

Doi, M., Thyboll, J., Kortesmaa, J., Jansson, K., Iivanainen, A., Parvardeh, M., Timpl, R., Hedin, U., Swedenborg, J. and Tryggvason, K. (2002). Recombinant human laminin-10 (alpha5beta1gamma1). Production, purification, and migration-promoting activity on vascular endothelial cells. *J. Biol. Chem.* **277**, 12741-12748.

Gao, Y., Dickerson, J. B., Guo, F., Zheng, J. and Zheng, Y. (2004). Rational design and characterization of a Rac GTPase-specific small molecule inhibitor. *Proc. Natl. Acad. Sci. USA* **101**, 7618-7623.

Gao, L., McBeath, R. and Chen, C. S. (2010). Stem cell shape regulates a chondrogenic versus myogenic fate through Rac1 and N-cadherin. *Stem Cells* **28**, 564-572.

Ghaedi, M., Soleimani, M., Shabani, I., Duan, Y. and Lotfi, A. S. (2012). Hepatic differentiation from human mesenchymal stem cells on a novel nanofiber scaffold. *Cell. Mol. Biol. Lett.* **17**, 89-106.

Greiner, T. U., Kesavan, G., Ståhlberg, A. and Semb, H. (2009). Rac1 regulates pancreatic islet morphogenesis. *BMC Dev. Biol.* **9**, 2.

Hashemi, S. M., Soudi, S., Shabani, I., Naderi, M. and Soleimani, M. (2011). The promotion of stemness and pluripotency following feeder-free culture of embryonic stem cells on collagen-grafted 3-dimensional nanofibrous scaffold. *Biomaterials* **32**, 7363-7374.

Heasman, S. J. and Ridley, A. J. (2008). Mammalian Rho GTPases: new insights into their functions from in vivo studies. *Nat. Rev. Mol. Cell Biol.* **9**, 690-701.

Heller, H., Gredinger, E. and Bengal, E. (2001). Rac1 inhibits myogenic differentiation by preventing the complete withdrawal of myoblasts from the cell cycle. *J. Biol. Chem.* **276**, 37307-37316.

Higuchi, Y., Shiraki, N., Yamane, K., Qin, Z., Mochitate, K., Araki, K., Senokuchi, T., Yamagata, K., Hara, M., Kume, K. et al. (2010). Synthesized basement membranes direct the differentiation of mouse embryonic stem cells into pancreatic lineages. *J. Cell Sci.* **123**, 2733-2742.

Hunziker, L., Benitah, S. A., Braun, K. M., Jensen, K., McNulty, K., Butler, C., Potton, E., Nye, E., Boyd, R., Laurent, G. et al. (2011). Rac1 deletion causes thymic atrophy. *PLoS ONE* **6**, e19292.

Jung, J. (1999). Initiation of mammalian liver development from endoderm by fibroblast growth factors. *Science* **284**, 1998-2003.

Kamiya, A., Kinoshita, T., Ito, Y., Matsui, T., Morikawa, Y., Senba, E., Nakashima, K., Taga, T., Yoshida, K., Kishimoto, T., et al. (1999). Fetal liver development requires a paracrine action of oncostatin M through the gp130 signal transducer. *EMBO J.* **18**, 2127-2136.

Katsumoto, K., Shiraki, N., Miki, R. and Kume, S. (2010). Embryonic and adult stem cell systems in mammals: ontology and regulation. *Dev. Growth Differ.* **52**, 115-129.

Kazemnejad, S., Allameh, A., Soleimani, M., Gharehbaghian, A., Mohammadi, Y., Amirizadeh, N. and Jazayery, M. (2009). Biochemical and molecular characterization of hepatocyte-like cells derived from human bone marrow mesenchymal stem cells on a novel three-dimensional biocompatible nanofibrous scaffold. *J. Gastroenterol. Hepatol.* **24**, 278-287.

Kubo, A., Shinozaki, K., Shannon, J. M., Kouskoff, V., Kennedy, M., Woo, S., Fehling, H. J. and Keller, G. (2004). Development of definitive endoderm from embryonic stem cells in culture. *Development* **131**, 1651-1662.

Lee, Y. M., Lee, J. O., Jung, J.-H., Kim, J. H., Park, S.-H., Park, J. M., Kim, E.-K., Suh, P.-G. and Kim, H. S. (2008). Retinoic acid leads to cytoskeletal rearrangement through AMPK-Rac1 and stimulates glucose uptake through AMPK-p38 MAPK in skeletal muscle cells. *J. Biol. Chem.* **283**, 33969-33974.

Leone, D. P., Srinivasan, K., Brakebusch, C. and McConnell, S. K. (2010). The rho GTPase Rac1 is required for proliferation and survival of progenitors in the developing forebrain. *Dev. Neurobiol.* **70**, 659-678.

Lim, S. H. and Mao, H.-Q. (2009). Electrospun scaffolds for stem cell engineering. *Adv. Drug Deliv. Rev.* **61**, 1084-1096.

Lim, S. H., Liu, X. Y., Song, H., Yarema, K. J. and Mao, H.-Q. (2010). The effect of nanofiber-guided cell alignment on the preferential differentiation of neural stem cells. *Biomaterials* **31**, 9031-9039.

Ma, K., Chan, C. K., Liao, S., Hwang, W. Y. K., Feng, Q. and Ramakrishna, S. (2008). Electrospun nanofiber scaffolds for rapid and rich capture of bone marrow-derived hematopoietic stem cells. *Biomaterials* **29**, 2096-2103.

Maddala, R., Chauhan, B. K., Walker, C., Zheng, Y., Robinson, M. L., Lang, R. A. and Rao, P. V. (2011). Rac1 GTPase-deficient mouse lens exhibits defects in shape, suture formation, fiber cell migration and survival. *Dev. Biol.* **360**, 30-43.

Malliri, A., Rygiel, T. P., van der Kammen, R. A., Song, J. Y., Engers, R., Hurlstone, A. F., Clevers, H. and Collard, J. G. (2006). The rac activator Tiam1 is a Wnt-responsive gene that modifies intestinal tumor development. *J. Biol. Chem.* **281**, 543-548.

Mfopou, J. K., Chen, B., Mateizel, I., Sermon, K. and Bouwens, L. (2010). Noggin, retinoids, and fibroblast growth factor regulate hepatic or pancreatic fate of human embryonic stem cells. *Gastroenterology* **138**, 2233–2245, 2245.e1-14.

Nikolova, E., Mitev, V., Minner, F., Deroanne, C. F. and Poumay, Y. (2008). The inhibition of the expression of the small Rho GTPase Rac1 induces differentiation with no effect on cell proliferation in growing human adult keratinocytes. *J. Cell. Biochem.* **103**, 857-864.

Nobes, C. D. and Hall, A. (1995). Rho, rac, and cdc42 GTPases regulate the assembly of multimolecular focal complexes associated with actin stress fibers, lamellipodia, and filopodia. *Cell* **81**, 53-62.

Nur-E-Kamal, A., Ahmed, I., Kamal, J., Schindler, M. and Meiners, S. (2005). Three dimensional nanofibrillar surfaces induce activation of Rac. *Biochem. Biophys. Res. Commun.* **331**, 428-434.

Nur-E-Kamal, A., Ahmed, I., Kamal, J., Schindler, M. and Meiners, S. (2006). Three-dimensional nanofibrillar surfaces promote self-renewal in mouse embryonic stem cells. *Stem Cells* **24**, 426-433.

Purcell, E. K., Naim, Y., Yang, A., Leach, M. K., Velkey, J. M., Duncan, R. K. and Corey, J. M. (2012). Combining topographical and genetic cues to promote neuronal fate specification in stem cells. *Biomacromolecules* **13**, 3427-3438.

Ridley, J., Paterson, H. F., Johnston, C. L., Diekmann, D. and Hall, A. (1992). The small GTP-binding protein rac regulates growth factor-induced membrane ruffling. *Cell* **70**, 401-410.

Rossi, J. M., Dunn, N. R., Hogan, B. L. and Zaret, K. S. (2001). Distinct mesodermal signals, including BMPs from the septum transversum mesenchyme, are required in combination for hepatogenesis from the endoderm. *Genes Dev.* **15**, 1998-2009.

Schindler, M., Nur-E-Kamal, A. and Ahmed, I. (2006). Living in three dimensions. *Cell Biochem.* **45**, 215-227.

Schindler, M., Ahmed, I., Kamal, J., Nur-E-Kamal, A., Grafe, T. H., Young Chung, H. and Meiners, S. (2005). A synthetic nanofibrillar matrix promotes in vivo-like organization and morphogenesis for cells in culture. *Biomaterials* **26**, 5624-5631.

Schmidt, C., Bladt, F., Goedecke, S., Brinkmann, V., Zschiesche, W., Sharpe, M., Gherardi, E. and Birchmeier, C. (1995). Scatter factor/hepatocyte growth factor is essential for liver development. *Nature* **373**, 699-702.

Shih, Y.-R. V., Chen, C.-N., Tsai, S.-W., Wang, Y. J. and Lee, O. K. (2006). Growth of mesenchymal stem cells on electrospun type I collagen nanofibers. *Stem Cells* **24**, 2391-2397.

Shin, D., Shin, C. H., Tucker, J., Ober, E. A., Rentzsch, F., Poss, K. D., Hammerschmidt, M., Mullins, M. C. and Stainier, D. Y. (2007). Bmp and Fgf signaling are essential for liver specification in zebrafish. *Development* **134**, 2041-2050.

Shiraki, N., Yoshida, T., Araki, K., Umezawa, A., Higuchi, Y., Goto, H., Kume, K. and Kume, S. (2008a). Guided differentiation of embryonic stem cells into Pdx1-expressing regional-specific definitive endoderm. *Stem Cells* **26**, 874-885.

Shiraki, N., Umeda, K., Sakashita, N., Takeya, M., Kume, K. and Kume, S. (2008b). Differentiation of mouse and human embryonic stem cells into hepatic lineages. *Genes Cells* **13**, 731-746.

Shiraki, N., Yamazoe, T., Qin, Z., Ohgomori, K., Mochitate, K., Kume, K. and Kume, S. (2011). Efficient differentiation of embryonic stem cells into hepatic cells in vitro using a feeder-free basement membrane substratum. *PLoS ONE* **6**, e24228.

Si-Tayeb, K., Noto, F. K., Nagaoka, M., Li, J., Battle, M. A., Duris, C., North, P. E., Dalton, S. and Duncan, S. A. (2010). Highly efficient generation of human hepatocyte-like cells from induced pluripotent stem cells. *Hepatology* **51**, 297-305.

Sonnenberg, E., Meyer, D., Weidner, K. M. and Birchmeier, C. (1993). Scatter factor/hepatocyte growth factor and its receptor, the c-met tyrosine kinase, can mediate a signal exchange between mesenchyme and epithelia during mouse development. *J. Cell Biol.* **123**, 223-235.

Stappenbeck, T. S. and Gordon, J. I. (2000). Rac1 mutations produce aberrant epithelial differentiation in the developing and adult mouse small intestine. *Development* **127**, 2629-2642.

Suemori, H., Yasuchika, K., Hasegawa, K., Fujioka, T., Tsuneyoshi, N. and Nakatsuji, N. (2006). Efficient establishment of human embryonic stem cell lines and long-term maintenance with stable karyotype by enzymatic bulk passage. *Biochem. Biophys. Res. Commun.* **345**, 926-932.

Sugihara, K., Nakatsuji, N., Nakamura, K., Nakao, K., Hashimoto, R., Otani, H., Sakagami, H., Kondo, H., Nozawa, S., Aiba, A. et al. (1998). Rac1 is required for the formation of three germ layers during gastrulation. *Oncogene* **17**, 3427-3433.

Tremblay, K. D., Hoodless, P. A., Bikoff, E. K. and Robertson, E. J. (2000). Formation of the definitive endoderm in mouse is a Smad2-dependent process. *Development* **127**, 3079-3090.

Umeda, K., Suzuki, K., Yamazoe, T., Shiraki, N., Higuchi, Y., Tokieda, K., Kume, K., Mitani, K. and Kume, S. (2013). Albumin gene targeting in human embryonic stem cells and induced pluripotent stem cells with helper-dependent adenoviral vector to monitor hepatic differentiation. *Stem Cell Res.* **10**, 179-194.

Varon, C., Rottiers, P., Ezan, J., Reuzeau, E., Basoni, C., Kramer, I. and Génot, E. (2008). TGFbeta1 regulates endothelial cell spreading and hypertrophy through a Rac-p38-mediated pathway. *Biol. Cell* **100**, 537-550.

Woo, S., Housley, M. P., Weiner, O. D. and Stainier, D. Y. R. (2012). Nodal signaling regulates endodermal cell motility and actin dynamics via Rac1 and Prex1. *J. Cell Biol.* **198**, 941-952.

Xie, J., Willerth, S. M., Li, X., Macewan, M. R., Rader, A., Sakiyama-Elbert, S. E. and Xia, Y. (2009). The differentiation of embryonic stem cells seeded on electrospun nanofibers into neural lineages. *Biomaterials* **30**, 354-362.

Tissue and Cell 45 (2013) 407–413

Contents lists available at ScienceDirect

Tissue and Cell

journal homepage: www.elsevier.com/locate/tice

Short communication

Investigation of telomere length dynamics in induced pluripotent stem cells using quantitative fluorescence *in situ* hybridization

Masanori Terai[a,b,*], Naotaka Izumiyama-Shimomura[a], Junko Aida[a], Naoshi Ishikawa[a], Mie Kuroiwa[c], Steven S.S. Poon[d], Tomio Arai[e], Masashi Toyoda[f], Hidenori Akutsu[g], Akihiro Umezawa[g], Ken-ichi Nakamura[a], Kaiyo Takubo[a,**]

[a] Research Team for Geriatric Pathology, Tokyo Metropolitan Institute of Gerontology, Tokyo 173-0015, Japan
[b] Department of Judotherapy, Faculty of Health Sciences, Tokyo Ariake University of Medical and Health Sciences, Tokyo 135-0063, Japan
[c] Department of Pathophysiology, Yokohama College of Pharmacy, Yokohama 245-0066, Japan
[d] Terry Fox Laboratory, British Columbia Cancer Research Centre, Vancouver, BC, Canada
[e] Department of Pathology, Tokyo Metropolitan Geriatric Hospital, Tokyo 173-0015, Japan
[f] Research Team for Vascular Medicine, Tokyo Metropolitan Institute of Gerontology, Tokyo 173-0015, Japan
[g] Department of Reproductive Biology, National Research Institute for Child Health and Development, Tokyo 157-8535, Japan

ARTICLE INFO

Article history:
Received 30 April 2013
Received in revised form 8 July 2013
Accepted 8 July 2013
Available online 5 August 2013

Keywords:
Telomere
iPSC
Q-FISH
Chromosome
Karyotype analysis

ABSTRACT

Here we attempted to clarify telomere metabolism in parental cells and their derived clonal human induced pluripotent stem cells (iPSCs) at different passages using quantitative fluorescence *in situ* hybridization (Q-FISH). Our methodology involved estimation of the individual telomere lengths of chromosomal arms in individual cells within each clone in relation to telomere fluorescence units (TFUs) determined by Q-FISH. TFUs were very variable within the same metaphase spread and within the same cell. TFUs of the established iPSCs derived from human amnion (hAM933 iPSCs), expressed as mean values of the median TFUs of 20 karyotypes, were significantly longer than those of the parental cells, although the telomere extension rates varied quite significantly among the clones. Twenty metaphase spreads from hAM933 iPSCs demonstrated no chromosomal instability. The iPSCs established from fetal lung fibroblasts (MRC-5) did not exhibit telomere shortening and chromosomal instability as the number of passages increased. However, the telomeres of other iPSCs derived from MRC-5 became shorter as the number of passages increased, and one (5%) of 20 metaphase spreads showed chromosomal abnormalities including X trisomy at an early stage and all 20 showed abnormalities including X and 12 trisomies at the late stage.

1. Introduction

Telomeres are repetitive G-rich DNA sequences found at the ends of linear eukaryotic chromosomes and appear to play a key role in preventing genomic instability (Blackburn, 2001; de Lange, 2005). Telomeres in human cells show shortening due mainly to mitosis *in vitro* (Vaziri et al., 1994), and aging *in vivo* (Aida et al., 2008). Telomere lengths of cultured fibroblasts (Takubo et al., 2010) and human tissues (Aida et al., 2008) show marked heterogeneity among individual telomeres and in terms of mean or median values in individual cells. Telomere length heterogeneity and telomerase expression among induced pluripotent stem cells (iPSCs) have been reported previously (Wang et al., 2012).

iPSCs are derived from somatic cells and, like embryonic stem cells, possess the capacity to differentiate into cell derivatives of all three germ layers (Takahashi and Yamanaka, 2006; Takahashi et al., 2007). iPSCs have been generated from somatic cells derived from aged organisms, including both mouse and human (Takahashi and Yamanaka, 2006; Takahashi et al., 2007). iPSCs have considerable therapeutic promise, as well as providing a potent *in vitro* model for studying biological processes (Apostolou and Hochedlinger, 2011). It has been reported that direct reprogramming of somatic cells to a pluripotent condition is accompanied by telomerase activation and telomere elongation (Park et al., 2008; Takahashi and Yamanaka, 2006; Takahashi et al., 2007). However, there is very little detailed information about telomere metabolism in individual iPSCs.

Studies using Southern blotting (Takahashi et al., 2007) or semi-quantitative fluorescence *in situ* hybridization (FISH) (Suhr et al.,

* Corresponding author at: Department of Judotherapy, Faculty of Health Sciences, Tokyo Ariake University of Medical and Health Sciences, 2-9-1 Ariake, Koto-ku, Tokyo 135-0063, Japan. Tel.: +81 3 6703 7061; fax: +81 3 6703 7061.
** Corresponding author. Fax: +81 3 3579 4776.
E-mail addresses: terai@tau.ac.jp, teramasa@agate.plala.or.jp (M. Terai), Takubo@tmig.or.jp (K. Takubo).

0040-8166/$ – see front matter © 2013 Elsevier Ltd. All rights reserved.
http://dx.doi.org/10.1016/j.tice.2013.07.003

2009) have indicated that some iPSCs may display significantly elongated telomeres, whereas telomere elongation or shortening may be evident in some lines but not in others. Terminal restriction fragment (TRF) analysis by Southern blotting does not estimate pure telomere length due to the fact that the TRF has subtelomere components (Aubert et al., 2012). iPSCs are usually cultured on feeder cells (irradiated mouse cells), and therefore the samples obtained are always admixtures of iPSCs and feeder cells, making it difficult to obtain DNA from pure iPSCs after multiple passages. Accordingly, instead of Southern blotting, we have used the quantitative fluorescence *in situ* hybridization (Q-FISH) method to measure iPSC telomere length.

We have also measured individual telomere lengths of chromosomal arms in human fibroblast strains by Q-FISH to clarify the morphologic signs of chromosomal instability (Takubo et al., 2010). Our findings indicated a linear correlation between telomere fluorescence units (TFUs) estimated by Q-FISH and telomere length measured by Southern blotting (Takubo et al., 2010). Few previous studies have attempted to examine telomere metabolism in human iPSCs after various numbers of passages or in quantitative terms using an assay such as Q-FISH (Liu et al., 2012). Here, therefore, using Q-FISH, we attempted to clarify the telomere metabolism of iPSCs and the parental cells from which they were derived at different passages using cloned iPSCs. In terms of the linear correlation between TFUs determined by Q-FISH, we estimated telomere lengths of individual cells by measuring the TFUs of telomere lengths of chromosomal arms in individual cells.

2. Materials and methods

2.1. Ethics statement

Human amnion cells were collected by scraping tissue from surgical specimens, with signed informed consent from the donors concerned, and under ethical approval from the Institutional Review Board of the National Institute for Child Health and Development, Japan. The surgical specimens were irreversibly de-identified. All experiments involving the handling of human cells and tissues were performed in line with tenets of the Declaration of Helsinki.

2.2. Human cell culture

Human amniotic membrane (hAM)-derived cells were independently established in our laboratory (Cui et al., 2007, 2011; Nishino et al., 2010, 2011). hAM-derived cells and MRC-5 cells were maintained in Dulbecco's Modified Eagle Medium (DMEM) supplemented with 10% fetal bovine serum and penicillin–streptomycin. Human iPSCs were generated in our laboratory using the procedures described by Yamanaka and colleagues (Cui et al., 2007, 2011; Nishino et al., 2010, 2011; Takahashi and Yamanaka, 2006; Takahashi et al., 2007). The iPSCs were established from hAM-derived cells and MRC-5, and designated hAM933 iPSCs and MRC-5 iPSCs, respectively. They were maintained on irradiated mouse embryonic fibroblasts (MEFs) in iPSellon medium (Cardio Incorporated, Kobe, Japan) supplemented with 10 ng/ml recombinant human basic fibroblast growth factor (bFGF, Wako Pure Chemical Industries, Ltd., Osaka, Japan). We used iPSCs that had been chosen randomly from stable lines in our laboratory.

We measured telomere lengths in the parental cells (hAM933 and MRC-5), two iPSCs (hAM933 iPSCs-2, hAM933 iPSCs-3) derived from different colonies originating from hAM933, and two iPSCs (MRC-5 iPSCs-16 and MRC-5 iPSCs-40) cloned from the same iPSCs (MRC-5 iPSCs) at different passages (MRC-5 iPSCs-16; passages 22 and 59; MRC-5 iPSCs-40; passages 21 and 62) (Table 1).

3. Q-FISH and image analysis

3.1. Probes and counterstaining

For karyotype analysis and quantitative analysis of telomeres, metaphase chromosomes were fixed and then hybridized using the peptide nucleic acid-FISH preparation method described previously (Poon and Lansdorp, 2001a,b).

A Cy3-labeled $(CCCTAA)_3$ peptide nucleic acid probe (telo C) (Fasmac, Atsugi, Catalogue No. F1002, Japan) was used to label the telomeres, and a FITC-labeled CTTCGTTGGAAACGGGGT peptide nucleic acid probe (CENP1; a non-specific centromere probe; Fasmac, custom made, Japan) was used for labeling the centromere. The chromosome preparations were counterstained with 4′,6-diamidino-2-phenylindole (DAPI, Molecular Probes, Eugene, OR, USA).

3.2. Q-FISH and image analysis

Analysis of fluorescence images was performed as described previously (Takubo et al., 2010). Digital images were recorded with a CCD camera, AxioCam MRm (Zeiss, Oberkochen, Germany), mounted on an Axio Imager M1 (Zeiss) epifluorescence microscope equipped with a triple band-pass filter for Cy3/FITC/DAPI (61010 Chroma Technology, Corp., Rockingham, VT, USA) and a 63× oil objective lens (Zeiss EC Plan-NEOFLUAR 63×/1.25 ∞/0.17). Microscope control and image acquisition were performed with the ISIS system (MetaSystems, GmbH, Altlussheim, Germany).

The level of calibration was used to ensure a reliable quantitative estimation of telomere length in the various samples. To correct for daily variations in lamp intensity and alignment, images of fluorescent beads (orange beads, size 0.2 μm, Molecular Probes, Inc.) were acquired just prior to acquisition of the images from the samples. The fluorescence intensities of the beads and telomeres were analyzed using the TFLTelo-V2 software package (Terry Fox Laboratory, BC Cancer Research Centre, Canada).

3.3. Karyotype analysis using the iPSCs FISH samples

The parental cells and all of the iPSCs at early and late passages were subjected to karyotyping of 20 metaphase spreads of FISH samples using telomere measurements for detection of abnormalities (Table 1). Chromosome identification and karyotype designations were performed in accordance with the International System for Human Cytogenetic Nomenclature (Shaffer et al., 2009).

3.4. Measurements of telomere length in metaphase spreads

Using the ISIS karyotyping system, we analyzed the karyotypes of 20 metaphase spreads at early passage (hAM933, passage 3, MRC-5, and MRC-5 iPSCs-16 and 40, passages 22 and passages 21, respectively) and late passage (hAM933 iPSCs-2, passage 25, hAM933 iPSCs-3, passage 27, MRC-5 iPSCs-16, passage 59 and MRC-5 iPSCs-40, passage 62). We then measured the telomere fluorescence intensities of the p- and q-arms of all the chromosomes in the spread individually.

The median TFU value was defined as a representative value for a metaphase spread (184 telomeres), and the mean value of the median values for all metaphase spreads for a single subject was defined as the representative value for that subject. The mean value of the median for all subjects within each of the three groups was defined as the representative value for the subject group.

Table 1
Data for iPSCs, karyotype analyses, and telomere length measurements.

Cell (ID)	Origin	Passages	Karyotype	Mean of median TFU (SD)	Minimum TFU	Ratio after reprogramming and multiple PDL
hAM933	Amnion	3	46, XY[20]	13,936 (1526)	425	1.00
hAM933 iPSCs-2	Amnion	25	46, XY[20]	23,302 (3864)	568	1.67
hAM933 iPSCs-3	Amnion	27	46, XY[20]	19,309 (3334)	471	1.39
MRC-5	Fetal lung fibroblasts	–	46, XY[20]	14,010 (2015)	380	1.00
MRC-5 iPSCs-16	Fetal lung fibroblasts	22	46, XY[20]	19,670 (3501)	766	1.40
MRC-5 iPSCs-16	Fetal lung fibroblasts	59	46, XY[20]	18,613 (3147)	609	1.33
MRC-5 iPSCs-40	Fetal lung fibroblasts	21	46, XY[19],47, XY, +X[1]	25,092 (4384)	700	1.79
MRC-5 iPSCs-40	Fetal lung fibroblasts	62	46, XY, inc[5], 47, XY, +12[8], 47, XY, +mar[4], 47, XY, +X[2], 48, XY +2mar[1]	16,923 (4191)	371	1.21

TFU: telomere fluorescence units; mar: marker chromosome; inc: incomplete.

3.5. Statistical analysis

The telomere lengths in the two groups (parental cells and their iPSCs, and MRC-5 iPSCs-16 and 40 at early and late passages) were compared using the unpaired t test. Fisher's Z test and Pearson's correlation coefficient were used to compare any correlations. For all comparisons, differences at $p < 0.05$ were considered to be significant.

4. Results

4.1. Karyotype analysis

FISH images were obtained for the parental cells established from human amnion (hAM933) and fetal lung fibroblasts (MRC-5), and the iPSCs established from hAM933 and MRC-5, which were designated hAM933 iPSCs-2, hAM933 iPSCs-3, MRC-5 iPSCs-16

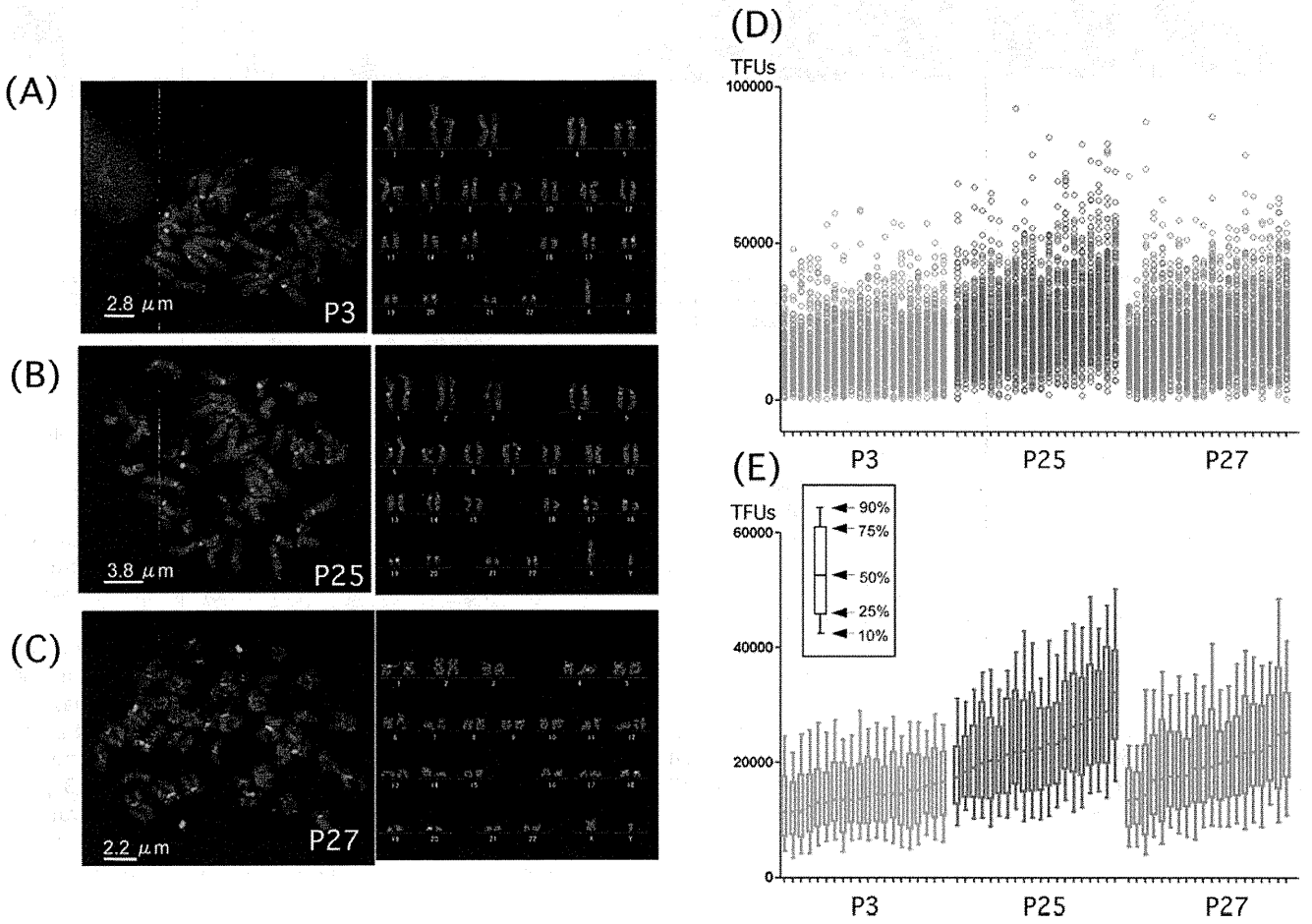

Fig. 1. Karyotype analysis and telomere length measured by Q-FISH and image analyses of hAM933 (A), hAM933 iPSCs-2 (B) and hAM933 iPSCs-3 (C), and telomere fluorescence units (TFUs, D and E) of the p- and q-arms of all constituent chromosomes. No chromosomal instabilities were found. Twenty metaphase spreads from the hAM933 parental cells (A, 3P; passage 3), hAM933 iPSCs-2 (B, 25P; passage 25) and hAM933 iPSCs-3 (C, 27P; passage 27). Cy3, FITC, and DAPI images were observed after assignment of pseudo-colors (red for Cy3, green for FITC and blue for DAPI). The labeling with Cy3 and FITC demonstrated the telomeres and centromeres, respectively. The chromosome preparations were counterstained with DAPI. The telomere fluorescence units (TFUs) of the p- and q-arms of all the chromosomes in the spread were measured individually. The median telomere lengths of 20 metaphase spreads in the parental cells (hAM933, passage 3), hAM933 iPSCs-2 (passage 25) and hAM933 iPSCs-3 (passage 27) are shown as scatter plots for all analyzed data (D) and as box plots (E).